Efficacy of CD40 Agonists Is Mediated by Distinct cDC Subsets and Subverted by Suppressive Macrophages

Aleksandar Murgaski[1,2], Máté Kiss[1,2], Helena Van Damme[1,2], Daliya Kancheva[1,2], Isaure Vanmeerbeek[3], Jiri Keirsse[1,2], Eva Hadadi[1,2], Jan Brughmans[1,2], Sana M. Arnouk[1,2], Ahmed E.I. Hamouda[1,2], Ayla Debraekeleer[1,2], Victor Bosteels[4,5], Yvon Elkrim[1,2], Louis Boon[6], Sabine Hoves[7], Niels Vandamme[8,9], Sofie Deschoemaeker[1,2], Sophie Janssens[4,5], Abhishek D. Garg[3], Greetje Vande Velde[10], Martina Schmittnaegel[7], Carola H. Ries[7], and Damya Laoui[1,2]

ABSTRACT

Agonistic αCD40 therapy has been shown to inhibit cancer progression in only a fraction of patients. Understanding the cancer cell–intrinsic and microenvironmental determinants of αCD40 therapy response is therefore crucial to identify responsive patient populations and to design efficient combinatorial treatments. Here, we show that the therapeutic efficacy of αCD40 in subcutaneous melanoma relies on preexisting, type 1 classical dendritic cell (cDC1)–primed $CD8^+$ T cells. However, after administration of αCD40, cDC1s were dispensable for antitumor efficacy. Instead, the abundance of activated cDCs, potentially derived from cDC2 cells, increased and further activated antitumor $CD8^+$ T cells. Hence, distinct cDC subsets contributed to the induction of αCD40 responses. In contrast, lung carcinomas, characterized by a high abundance of macrophages, were resistant to αCD40 therapy. Combining αCD40 therapy with macrophage depletion led to tumor growth inhibition only in the presence of strong neoantigens. Accordingly, treatment with immunogenic cell death–inducing chemotherapy sensitized lung tumors to αCD40 therapy in subcutaneous and orthotopic settings. These insights into the microenvironmental regulators of response to αCD40 suggest that different tumor types would benefit from different combinations of therapies to optimize the clinical application of CD40 agonists.

Significance: This work highlights the temporal roles of different dendritic cell subsets in promoting $CD8^+$ T-cell–driven responses to CD40 agonist therapy in cancer.

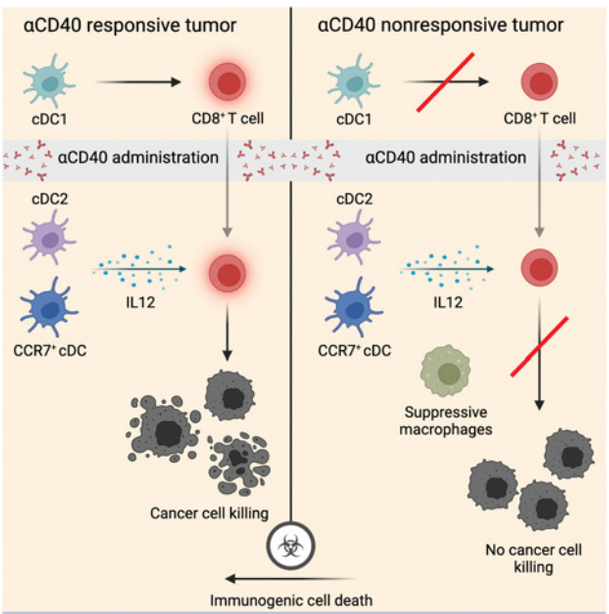

Dendritic cell subsets have distinct roles in promoting $CD8^+$ T-cell–driven responses to αCD40, which can be enhanced by immunogenic cell death–inducing chemotherapy.

Introduction

Effective treatment of many cancer types consistently improved over recent decades (1). Despite checkpoint inhibitors cementing themselves as invaluable therapeutic interventions, only a minority of patients experience long-term efficacy (2). Therefore, identification of prognostic biomarkers and synergistic combination therapies that can increase the proportion of responsive patients are current focuses at the forefront of tumor immunology research (3).

Alternative therapies that aim to prime T cells rather than rescue dysfunctional T cells show great promise (4). The TNF-receptor superfamily member CD40 is an ideal target within this context, as CD40 ligation that occurs naturally during T-cell help via CD40-L results in the activation of antigen-presenting cells leading to

[1]Myeloid Cell Immunology Lab, VIB Center for Inflammation Research, Brussels, Belgium. [2]Lab of Cellular and Molecular Immunology, Vrije Universiteit Brussel, Brussels, Belgium. [3]Laboratory of Cell Stress & Immunity (CSI), Department of Cellular & Molecular Medicine, KU Leuven, Leuven, Belgium. [4]Laboratory for ER stress and Inflammation, VIB Center for Inflammation Research, Ghent, Belgium. [5]Department of Internal Medicine and Pediatrics, Ghent University, Ghent, Belgium. [6]JJP Biologics, Warsaw, Poland. [7]Roche Pharmaceutical Research and Early Development, Discovery Oncology, Roche Innovation Center Munich, Penzberg, Germany. [8]Data Mining and Modeling for Biomedicine, VIB Center for Inflammation Research, Ghent, Belgium. [9]Department of Applied Mathematics, Computer Science and Statistics, Ghent University, Ghent, Belgium. [10]Department of Imaging and Pathology, Faculty of Medicine, KU Leuven, Leuven, Belgium.

Current address for Carola H. Ries: Dr. Carola Ries Consulting, Penzberg, Germany.

Corresponding Author: Damya Laoui, Lab of Cellular and Molecular Immunology, Pleinlaan 2, B-1050, Brussels, Belgium. E-mail: dlaoui@vub.be

Cancer Res 2022;82:3785–801

doi: 10.1158/0008-5472.CAN-22-0094

increased T-cell priming (5–8). Preclinical results using CD40 agonist antibodies have been shown to slow the growth of murine tumors containing strong tumor antigens (9, 10), however their success in the clinic as a monotherapy was limited to a minority of patients with melanoma (11). An encouraging aspect of CD40 agonist therapy lies in the broad potential for synergistic combinations that have been shown to reduce tumor growth, including antiangiogenic therapies, tumor-associated macrophage depletion, checkpoint inhibitors, chemotherapy, and radiotherapy (12–19). As such, CD40 agonists have achieved beneficial clinical outcomes in pancreatic cancer when combined with chemotherapy (20). Although the results of these combinations are encouraging, they also hint at the importance of understanding which combination of therapies should be applied in which context.

Most antitumor effects of CD40 agonists have been shown to rely on the function of $CD8^+$ T cells. However, critical cellular mediators must have activated these $CD8^+$ T-cell responses. The prime candidate that has been identified as critical to CD40 efficacy are type 1 conventional dendritic cells (cDC1) that are essential for $CD8^+$ T-cell priming (18, 21, 22). However, studies have also implicated macrophages and other monocyte-derived cells as critical components of successful CD40 agonist-mediated antitumor immunity (23, 24). Encouraging combinations investigated so far involve Flt3L treatment-mediated DC boosting therapies prior to CD40 agonist therapy, with or without radiotherapy, which have been able to slow tumor growth of orthotopic and subcutaneously implanted pancreatic ductal adenocarcinoma tumors, respectively (25, 26).

Altogether, these results underline the importance of understanding both the cancer- and immune-specific contexture, relating to successful CD40 agonist therapy. To shed further light on how the tumor microenvironments predict optimal responses to CD40 agonist therapy, and which combinatory interventions can resensitize nonresponsive tumors, in this study we performed single-cell RNA (scRNA-seq) sequencing on tumor-infiltrating immune cells to identify the cellular mediators of anti-CD40 (αCD40) therapy. We also utilized the *Xcr1*$^{wt/dtr}$ mouse model to temporally deplete cDC1s and show that whereas the therapeutic effect of αCD40 therapy in B16F10 tumors relied on the initial function of cDC1s prior to therapy, cDC2s could be responsible for the subsequent activation, but not expansion, of antitumor T cells in response to αCD40 therapy. When comparing the αCD40-responsive B16F10 melanoma with the αCD40-resistant Lewis lung carcinoma (LLC), we identified that the highly immunosuppressive microenvironment of LLC tumors as well as their poor immunogenicity limited αCD40 efficacy. By reducing suppression through αCSF1R treatment and increasing immunogenicity by combination with immunogenic cell death (ICD)-inducing chemotherapy, we could resensitize subcutaneous and orthotopic LLC tumors to αCD40 therapy.

Materials and Methods

Mouse strains

Female C57BL/6 mice were purchased from Janvier. *Xcr1*$^{wt/dtr}$ mice were provided by Christian Kurts (University of Bonn) with the permission of Tsuneyasu Kaisho. *Csf3r*$^{-/-}$ mice were provided by Sebastian Jaillon and Paola Allavena (Humanitas University). CD45.1 mice were purchased from Charles River. *Itgax*-DTR mice were obtained from in-house breeding. In all experiments involving transgenic or knockout mice, wild-type (+/+) littermate mice were used as controls as specified in the figures and figure legends.

All procedures followed the guidelines of the Belgian Council for Laboratory Animal Science and were approved by the Ethical Committee for Animal Experiments of the Vrije Universiteit Brussel (licenses 16–220–02, 18–220–19, 19–220–33, 20–220–32, 21–220–25, 22–220–12) and the Animal Ethics Committee of KU Leuven (ECD project P073/2022).

Bone marrow chimera generation

For the generation of bone marrow chimeras, female 6-week-old CD45.1 mice were lethally irradiated (8 Gy). After a six-hour rest period the mice were injected intravenously with 1.3×10^6 BM cells obtained from *Itgax*-WT or *Itgax*-DTR littermate mice. The mice were used experimentally 8 weeks after BM reconstitution. Chimerism was confirmed by flow cytometry prior to tumor challenge and treatment.

Tumor models

LLC and B16F10 cell lines (from ATCC) were cultured in DMEM (Gibco) supplemented with 10% (v/v) heat-inactivated FCS (Capricorn Scientific), 300 μg/mL L-glutamine, 100 units/mL penicillin, and 100 μg/mL streptomycin. For the LLC-OVA (a kind gift from Dmitry Gabrilovich) cell line, DMEM was replaced by RPMI (Gibco).

For subcutaneous tumor implantation, 10^6 LLC cells, 10^6 B16F10, or 3×10^6 LLC-OVA cells were injected subcutaneously into the right flank of syngeneic female C57BL/6 mice in 200 μL of Hank's Balanced Salt Solution (HBSS). For intravenous tumor injection, 0.25×10^6 LLC-OVA or LLC cells were injected into the tail vain of syngeneic female C57BL/6 mice in a 100 μL volume of HBSS.

Tumor volumes were determined by caliper measurements and calculated using the formula: $V = \pi \times (d^2 \times D)/6$, where d is the shortest diameter and D is the longest diameter.

Treatments

For CD40 agonist treatments, a single dose of 100 μg of αCD40 (clone: FGK4.5; BioXCell) agonist antibody or rat IgG2a isotype control (clone 2A3; BioXCell) was administered intraperitoneally in a volume of 100 μL HBSS when tumors reached approximately 100 mm^3.

For macrophage depletions, 660 μg of αCSF1R (clone 2G2; provided by Roche) or murine IgG1 isotype control (clone MOPC-21; BioXCell) were administered intraperitoneally in a volume of 100 μL HBSS when tumors reached approximately 100 mm^3 with additional doses being administered weekly, if applicable.

For B-cell depletions, 500 μg of αCD20 (clone 18B12; BioXCell) or murine IgG2a (clone 2A3; BioXCell) were administered intraperitoneally in a volume of 100 μL HBSS once at day 4 after tumor implantation.

To deplete cDC1s in *Xcr1*$^{wt/dtr}$ mice, diphtheria toxin (D0564, Merck) was injected intraperitoneally in *Xcr1*$^{wt/wt}$ and *Xcr1*$^{wt/dtr}$ mice at a dose of 25 ng/g body weight for the first dose, with following doses administered at a dose of 5 ng/g body weight.

For $CD8^+$ T-cell depletions, 200 μg of αCD8 (clone YTS169; Polpharma Biologics) was administered intraperitoneally in a volume of 100 μL HBSS every 2 to 3 days starting 1 day prior to tumor implantation.

For IL12 neutralization, 500 μg of αIL12 p40 (clone C17.8, BioXCell) or rat IgG2a (clone 2A3: BioXCell) was administered intraperitoneally in a volume of 100 μL HBSS daily starting 24 hours prior to αCD40 treatment and continuing until the end of the experiment.

To increase cDC numbers, 30 μg of Flt3L-Ig (hum/hum; clone Flt3L Fc-G1; BioXCell) was administered intraperitoneally in a volume

of 50 μL HBSS every 24 hours between day 0 and day 8 post-LLC tumor implantation.

To deplete Tregs, 100 μg of αCD25 (ONCC4, kindly provided by Oncurious) was administered intraperitoneally in a volume of 100 μL HBSS every 48 hours between day 4 and day 10 after LLC tumor implantation, unless otherwise indicated.

Neutrophils were depleted using 75 μg αLy6G (clone 1A8; BioXCell) followed by 150 μg mouse anti-RAT (clone MAR18.5; BioXCell) administered intraperitoneally in volumes of 100 μL HBSS. Alternatively, neutrophils were depleted using a CXCR2 inhibitor (SB225002; Selleck Chemicals) administered intraperitoneally at a dosage of 4 mg/kg body weight.

Oxaliplatin (NSC 266046; Selleck Chemicals) was dissolved in HBSS containing 5% glucose and administered intraperitoneally at 1 mg/kg body weight every 48 hours between day 4 and day 14 after LLC tumor implantation. Vehicle control (5% glucose in HBSS) was administered according to body weight of mice at time of treatment. Volumes administered were equal to 2 μL × weight of mouse (g).

Blood collection and tissue dissociation

Blood was collected from mice in 1 mL syringes containing 0.5 mol/L EDTA. Tumors were excised, cut in small pieces, incubated with 10 U/mL collagenase I, 400 U/mL collagenase intravenously and 30 U/mL DNase I (Worthington) in RPMI for 20 minutes at 37°C, squashed, triturated, and filtered on a 70 μm cell strainer. Spleens were mashed through a 70 μm cell strainer, bone marrow was flushed out from the femurs into RPMI. Single-cell suspensions were then treated with ammonium–chloride–potassium (ACK) erythrocyte lysis buffer.

Flow cytometry and cell sorting

Single cell suspensions were resuspended in HBSS and samples for flow cytometry analysis were incubated with Fixable Viability Dye eFluor 506 (1:1,000, eBioscience) for 30 minutes at 4°C. Next, cell suspensions were washed with HBSS and resuspended in HBSS with 2 mmol/L EDTA and 1% (v/v) FCS. To prevent nonspecific antibody binding to Fcγ receptors, cells were preincubated with anti-CD16/CD32 (clone 2.4G2) antibody. Cell suspensions were then incubated with fluorescently labeled antibodies diluted in HBSS with 2 mmol/L EDTA and 1% (v/v) FCS for 20 minutes at 4°C and then washed with the same buffer. The following fluorochrome-conjugated antibody clones were used: CD45 (30-F11), CD11b (M1/70), Ly6G (1A8), SiglecF (E50–2440), MHC-II (M5/114.15.2), Ly6C (HK1.4), F4/80 (CI:A3–1), CD11c (HL3), XCR1 (ZET), NK1.1 (PK136), CD19 (1D3), TCRβ (H57–597), CD4 (RM4–5), CD8α (53–6.7), CD44 (IM7), CD62 L (MEL-14), PD-1 (RMP1–30), CCR8 (REA921), MMR (C068C2), LAG-3 (C9B7W), CXCR2 (5E8/CXCR2), CD200 (OX2), CCR7 (4B12), MHC-I (SF1–1.1), SiglecH (551), Dextramer (Immudex, Catalog No. JD2163).

For intracellular staining, after extracellular staining was complete, samples were spun and fixed using the eBioscience Intracellular Fixation & Permeabilization Buffer Set (Thermo Fisher Scientific, 88–8824–00) according to manufacturer's instructions. The following fluorochrome-conjugated antibody clones were used: FoxP3 (FJK-16s), GZMB (GB11), Ki67 (16A8), ARG1 (14D2C43), and IL12p40 (C17.8). To measure active caspase-3 we used the FITC Active Caspase-3 Apoptosis Kit (BD Biosciences, 550480).

Flow cytometry data were acquired using a BD FACSCanto II (BD Biosciences) and analyzed using FlowJo. The gating strategy to identify immune cell populations in tumors is shown in Supplementary Fig. S1. Samples with cell contamination from the tumor-draining lymph node (identified as outliers in B-cell and naive T-cell abundance) were excluded from further analyses.

For fluorescence-activated cell sorting, 7AAD− $CD45^+$ immune populations were sorted into RPMI containing microcentrifuge tubes for single cell sequencing. For purification of tumor-residing neutrophils, samples were enriched for $CD11b^+$ cells using magnetic cell separation (Miltenyi). 7-AAD staining was used to exclude dead cells. Cell subsets were then sorted into ME medium [RPMI with 10% (v/v) FCS, 300 μg/mL L-glutamine, 100 units/mL penicillin, 100 μg/mL streptomycin, 1% (v/v) MEM nonessential amino acids (11140050, Gibco), 1 mmol/L sodium pyruvate (Gibco), and 0.02 mmol/L 2-mercaptoethanol (Sigma-Aldrich)]. Fluorescence-activated cell sorting was performed using a BD FACSAria II (BD Biosciences).

scRNA-seq and cellular indexing of transcriptomes and epitopes by sequencing

Similarly sized tumors (collected at either day 15 or day 17 after tumor inoculation for LLC or B16F10, respectively) were pooled from three mice. The regular tissue processing procedure was followed, with the addiction of actinomycin D (Sigma-Aldrich, A1410–5MG) to each buffer. Tumor collection was performed in 30 μmol/L, enzyme incubation and subsequent filtering in 15 μmol/L, and all other steps in 3 μmol/L. For scRNA-seq, the single cell suspensions were stained with APC-Cy7-labeled anti-CD45 and 7AAD. Approximately 60,000 live $CD45^+$ cells were sorted into ME medium using the BD FACSAria III (BD Biosciences). The sorted cells were centrifuged and resuspended in PBS containing 0.04% BSA at room temperature at an estimated final concentration of 1,000 cells/μL. The cellular indexing of transcriptomes and epitopes by sequencing (CITE-seq) sample was counted and 1 million cells were isolated and centrifuged. The pellet was resuspended and incubated for 30 minutes on ice with 25 μL of staining mix in PBS + 0.04% BSA containing APC-Cy7 labeled mouse anti-CD45 and the mouse cell surface protein antibody panel containing 174 oligo-conjugated antibodies. Subsequently the cells were washed and 60,000 live $CD45^+$ cells were sorted into ME medium. Next, the 10× genomics single-cell bead-in emulsions and scRNA-seq and CITE-seq libraries were prepared as described previously (27). The mean reads per cell for the LLC and B16F10 scRNA-seq data were 17,476 and 31,109, with a sequencing saturation metric of 38% and 42.7%, respectively. The LLC CITE-seq data yielded 11,624 mean RNA reads per cell, 28.4% RNA sequencing saturation, and 2,042 mean ADT reads per cell. For filtering of the low-quality cell barcodes, associated with empty droplets, the "emptyDrops" function of the DropletUtils package (v.1.8.0) has been applied on the RNA expression data, using an FDR cutoff of 0.01. The gene expression matrices were further filtered using the Scater package (v.1.16.2). The detection of outlier cells for percentage of mitochondrial genes per cell and removal of low-abundance genes were performed as described previously (28). Library size normalization and unsupervised Leiden clustering were performed with Seurat v.3.2.3. The obtained clustering was visualized in two-dimensional scatter plots via Uniform Manifold Approximation and Projection (UMAP). Differential expression analysis was done using Wilcoxon Rank Sum test with the "FindMarkers" function of Seurat to identify genes, specific for each cluster. Bonferroni correction has been applied for adjustment of the P values. The processing of the ADT expression matrix was done as described previously (28).

Trajectory inference

Trajectory inference was performed on the monocyte and TAM subsets of the mouse B16F10 and LLC tumors, using the Slingshot

package (v.1.8.0; ref. 29). The B16F10 and the LLC datasets were merged using the "merge" command of Seurat, then monocyte and TAM clusters were subsetted and clustered using the same procedure as described above. Slingshot was run on the first 10 PCA embeddings of the monocyte/TAM subset. To identify differentially expressed genes along the identified trajectories, the package tradeseq was used (v.1.4.0), using five knots for fitting the model. To find the genes that vary significantly between the two lineages, the "diffEndTest" was used, whereas for Identifying genes that change along a lineage, the "associationTest" function was applied (30).

Gene ontology

To predict the putative molecular pathways and functions of the genes that distinguish the B16F10 and LLC TAMs, we performed a GO analysis on the genes that varied significantly between the two lineages using the Metascape (http://metascape.org/) online tool with default parameters (31). We have selected the genes had Wald statistic >100 and LogFc >1.5 or LogFc < −1.5, respectively for the "diffEndTest" between lineage 1 and 2.

scRNA-seq public data of αCD40-treated MC38 mice

Zhang and colleagues analyzed $CD45^+$ sorted tumors and tumor-draining lymph nodes from MC38 tumor-bearing mice treated with αCD40 antibodies (32). We have extracted the raw FASTQ data of the day 2 treated MC38 tumors with αCD40 or isotype control (ERR3498977, ERR3499108, ERR3498975, ERR3499106, ERR3499107, ERR3499050, ERR3498978, ERR3499109, ERR3507081, ERR3507082) from https://www.ebi.ac.uk/ena/browser/view/PRJEB34105. The single cell data have been analyzed as described above. DC clusters have been subsetted and reclustered.

Micro-CT

Mice were anaesthetized with isoflurane (2% in 100% oxygen; Piramal Healthcare) and scanned in the supine position using *in vivo* μCT (Skyscan 1278; Bruker micro-CT) with the following parameters: 50 kVp X-ray source voltage, 350 μA current, 1 mm aluminum X-ray filter, 150 milliseconds exposure time per projection, acquisition of three projections per step was performed in 0.9° increments over a total of 220° angle, 10 cm field of view covering the whole body producing expiratory-weighted reconstructed data sets with 50 μm isotropic voxel size (33). Each scan took approximately 3 minutes and was associated with a measured radiation dose of 60 to 80 mGy (34).

Software provided by the manufacturer (TSort, NRecon, DataViewer, and CTan) was used to retrospectively gate, reconstruct, visualize, and process the μCT data. Quantification of nonaerated lung volume and total lung volume was carried out for a volume-of-interest covering the lung including the regions that had been manually delineated from coronal μCT images ensuring heart and main blood vessels were avoided (35, 36).

T-cell suppression assay

A total of 2×10^5 neutrophils sorted from tumors were added to 2×10^5 naïve C57BL/6 splenocytes stimulated with anti-CD3 (1 μg/mL) and anti-CD28 (2 μg/mL) and cultured in flat-bottom 96-well plates in ME medium for *ex vivo* cell culture described above. After 24 hours of culture, 1 μCi (0.037 MBq) ^{3}H-thymidine was added and after another 18 hours of culture, the plates were frozen and stored at −20°C, after which, T-cell proliferation was measured as count per minute in a liquid scintillation counter.

NF-κB and ISRE/IRF reporter assays

The J774 macrophage-like myeloid cells were cultured in a media containing 10% heat inactivated FBS. After two passages, J774 cells containing genetic reporter constructs for detecting transcriptional activity of the NF-κB and IFN-stimulated response element (ISRE)-binding IFN regulatory factor (IRF) were enriched via antibiotic-based selection (using 5 μg/mL blasticidin and 100 μg/mL of zeocin). The J774 NF-κB and ISRE/IRF reporter myeloid cells (Invivogen) were plated with a density of 3×10^4 cells per well in a 96-well plate. Cancer cells were plated in 10 cm dishes, and were treated with cisplatin (100 μmol/L), paclitaxel (100 μmol/L), doxorubicin (50 μmol/L), mitoxantrone (0.5 μmol/L), oxaliplatin (400 μmol/L), or left untreated. After 24 hours, the cancer cells were collected and counted. They were centrifuged at 15,000 rpm for 5 minutes and resuspended in J774 reporter myeloid media according to the manufacturer. These were then added on top of the J774 reporter myeloid cells, in a 1:1 ratio (in 200 μL final volume), within the 96-well plates. Stimulation with LPS (1,000 ng/mL) was used as a positive control. To measure the NF-κB transcriptional activity (marked by extracellular secretion of reporter alkaline phosphatase enzyme), after 24 or 48 hours of cancer cell-J774 coculture, 100 μL of media was transferred to a standard transparent-bottom 96-well plate. Herein, 100 μL of Quanti-BLUE substrate (Invivogen) for the alkaline phosphatase was added to each well and incubated for 4 to 8 hours. The absorbance was measured at an optical density of 655 nm with the Biotek Synergy H1M plate reader. To measure the ISRE/IRF expression (marked by extracellular secretion of reporter luciferase enzyme), another 100 μL of media was derived from the above cancer cell-J774 coculture in a white opaque-bottom 96-well plate. Herein, 50 μL of Quanti-LUC substrate (Invivogen) for the luciferase was added and bioluminescence was directly measured with 100 milliseconds of signal integration, with the Biotek Synergy H1M plate reader. To account for interassay baseline variability a fold change to the J774 myeloid cells alone was taken from all data derived from these reporter assays.

Schematic figures

All schematic figures were created using BioRender.com.

Statistical analysis

All graphs show mean ± SEM. Statistical significance (P value < 0.05) was determined in GraphPad Prism 9.1.2 software. For relevant pairwise comparisons, unpaired t tests were performed. For the comparison of multiple groups, one-way ANOVA was performed, followed by a posttest. Tumor growth curves were compared by mixed-effects two-way ANOVA with multiple comparisons tests, where appropriate statistical tests with Welch correction were performed. For statistically significant differences, the P value is indicated in graphs as the following: *, $P < 0.05$; **, $P < 0.01$; ***, $P < 0.001$; ****, $P < 0.0001$.

Data availability

The data associated with this study are available in the main text or the Supplementary Materials and Methods. scRNA-seq raw data are deposited at GEO (NCBI) under accession code GSE209763.

Results

CD40 agonist therapy repolarizes B16F10 tumors, resulting in reduced tumor growth

B16F10 melanoma is a frequently used preclinical mouse model in immuno-oncology that is highly infiltrated by immune cells (**Fig. 1A**),

of which, 13.0 ± 2.4% represent $CD8^+$ T cells (**Fig. 1B**; Supplementary Fig. S1A). To assess the activation status of the tumor-infiltrating $CD8^+$ T cells, we performed scRNA-seq on $CD45^+$ immune cells from B16F10 tumors grown subcutaneously in C57BL/6 mice. Unsupervised clustering yielded 19 distinct clusters, identified on the basis of their expression of canonical marker genes (**Fig. 1C**; Supplementary Fig. S1B). Interestingly, both defined $CD8^+$ T-cell clusters in B16F10 tumors expressed high levels of genes associated with an exhausted or dysfunctional T-cell phenotype including *Pdcd1* (PD-1), *Lag3* (CD223), and *Tox* (**Fig. 1D**). Anti-PD-1 mAb therapy has previously been shown to reinvigorate exhausted $CD8^+$ T cells, but likely due to low *Tcf7* (TCF7) expression in the $CD8^+$ T-cell population (**Fig. 1D**), did not result in delayed tumor growth in the B16F10 model (Supplementary Fig. S1C; refs. 37, 38), despite *Cd274* (PD-L1) gene expression within multiple different clusters (Supplementary Fig. S1D).

To investigate whether tumor growth could be arrested by targeting earlier steps in the tumor-immunity cycle, B16F10 tumor-bearing mice were treated with an anti-CD40 agonist antibody (αCD40; **Fig. 1E**), as CD40 was shown to enable DC licensing and maturation, resulting in subsequent priming of cytotoxic T cells (39). CD40 agonist monotherapy significantly reduced tumor growth and weight (**Fig. 1F** and **G**) whereas the relative infiltration of immune cells into B16F10 tumors increased (**Fig. 1H**). Ten days after αCD40 treatment, within the myeloid compartment, tumor-associated macrophages (TAM) were strongly decreased after successful αCD40 treatment, which is in line with previous observations showing that the presence of mature TAMs correlates with tumor size (40), whereas frequencies of cDC1 and cDC2 reduced slightly (**Fig. 1I–M**). Importantly, within the lymphocytes, the abundance of cytotoxic $CD8^+$ T cells was strongly increased compared with $CD4^+$ T cells, NK cells, and B cells (**Fig. 1N–Q**; Supplementary Fig. S1E and S1F), likely due to a higher proliferation rate (**Fig. 1R**). Moreover, in mice treated with αCD40, the $CD8^+$ T cells displayed an effector T-cell phenotype as indicated by the increased $CD44^+$ $CD62L^-$ effector versus $CD44^-$ $CD62L^+$ naive T-cell ratio (**Fig. 1S**). The elevated abundance of activated $CD8^+$ T cells was accompanied by both a decreased infiltration of $FoxP3^+$ regulatory T cells (Tregs), as well as a reduced expression of CCR8 on the Tregs (**Fig. 1T–U**), indicative for reduced suppressive phenotype of these cells (41). Collectively, these results indicate that CD40 agonist monotherapy is sufficient to repolarize the immune infiltrate in B16F10 tumors delaying tumor growth.

The effect of CD40 agonist in B16F10 tumors is independent of TAMs and B cells

To investigate the mechanisms underlying the reduced tumor growth upon αCD40 agonist treatment, we first set out to determine the impact of the increased abundance of cytotoxic $CD8^+$ T cells on the inhibition of tumor progression. Systemic depletion of $CD8^+$ T cells restored B16F10 tumor growth in αCD40 agonist treated mice to WT levels (**Fig. 2A**). Next, we interrogated our scRNA-seq data to assess which cell types were expressing *Cd40* and were potentially driving antitumor $CD8^+$ T-cell responses in B16F10 tumors. *Cd40* expression was mainly found in B cells, cDCs including cDC1s, cDC2s, $CCR7^+$ DCs [also termed migratory-DCs (MigDC), mature DCs, DC3 (42), or mregDCs (43)], and mononuclear myeloid cells including monocytes and different subsets of TAMs (**Fig. 2B**; Supplementary Fig. S2A). In accordance with the gene expression pattern, CD40 protein assessed via flow cytometry was only detected at the surface of $Ly6C^{high}$ monocytes, TAMs, cDC1s, cDC2s, and B cells within B16F10 tumors (**Fig. 2C**; Supplementary Fig. S2B).

Next, we investigated whether any of these populations are involved in the therapeutic effect of αCD40 treatment. B-cell depletion using αCD20 antibodies did not alter the reduced tumor growth upon αCD40 therapy and increased abundance of effector $CD8^+$ T cells (Supplementary Fig. S2C; **Fig. 2D–F**), indicating that the reduction in tumor growth mediated by the CD40 agonist was B-cell independent. Macrophage depletion using an αCSF1R antibody (Supplementary Fig. S2D) also did not revert the tumor growth, nor the increase in T-cell abundance and activation status or the decrease of immunosuppressive Tregs upon αCD40 therapy (Supplementary Fig. S2D; **Fig. 2G–K**), implying that the antitumor effect of CD40 agonist therapy was independent of TAMs.

The therapeutic effect of CD40 agonist in B16F10 tumors only partly relies on cDC1s

Having excluded the requirement of B cells and TAMs for the generation of a therapeutic response upon αCD40 treatment in B16F10, we next investigated the role of cDC1s. Hereto, we employed $Xcr1^{wt/dtr}$ mice, which allowed temporal control of systemic cDC1 depletion upon injection of diphtheria toxin (DT; Supplementary Fig. S3A–C; ref. 44). Strikingly, when cDC1 depletion was initiated 24 hours before αCD40 administration, the therapeutic effect of the CD40 agonist therapy was unaltered (**Fig. 3A**), suggesting that cDC1s did not play a major role in the αCD40-mediated immune response in established B16F10 tumors. Interestingly, in $Xcr1^{wt/dtr}$ mice, αCD40 treatment reduced the abundance of $CD8^+$ T cells to levels comparable with isotype-treated littermate control mice (**Fig. 3B**), highlighting the important role cDC1s play in increasing intratumoral $CD8^+$ T cells. Despite the inhibited expansion of $CD8^+$ T cells in $Xcr1^{wt/dtr}$ mice, the $CD8^+$ T cells still showed an effector T-cell phenotype in $Xcr1^{wt/dtr}$ mice treated with αCD40, with CD44:CD62 L ratio's and granzyme B secretion similar to the T cells in αCD40-treated littermate controls (**Fig. 3C**; Supplementary Fig. S3D). These suggest that cDC1s are essential for $CD8^+$ T-cell recruitment or expansion, whereas other cell types can also contribute to the proper activation of existing $CD8^+$ T cells into antitumor effector cells. Importantly, the depletion of these $CD8^+$ T cells in $Xcr1^{wt/dtr}$ mice treated with αCD40 agonist restored tumor growth in αCD40 treated mice to isotype-treated littermate control levels (**Fig. 3D**; Supplementary Fig. S3E). Overall, these findings suggest that therapeutic responses induced by αCD40 were driven by $CD8^+$ effector T cells, independent of cDC1-mediated activation. Indeed, when cDC1s were depleted 24 hours prior to tumor inoculation and depletion was maintained throughout tumor progression, the efficacy of αCD40 agonist therapy was abrogated (**Fig. 3E**). Consequently, only a nonsignificant trend towards higher $CD8^+$ T-cell levels was seen in αCD40-treated $Xcr1^{wt/dtr}$ mice, which was incapable of restricting B16F10 tumor growth (**Fig. 3F**).

Next, we aimed to unravel which other antigen-presenting cells were involved in the activation of existing $CD8^+$ T cells upon CD40 agonist therapy in the absence of cDC1s. Because TAMs expressed CD40 in B16F10 tumors and CD40-activated macrophages were shown to be involved in CD40-mediated tumor responses (23), we depleted TAMs in $Xcr1^{wt/dtr}$ mice (Supplementary Fig. S3f). The tumor progression and activation of $CD8^+$ T cells in this experiment did not differ from the results obtained in mice depleted of cDC1s 24 hours before αCD40 administration, in which TAMs were present, suggesting that TAMs were not responsible for $CD8^+$ T-cell activation in the absence of cDC1s (**Fig. 3G**; Supplementary Figs. S3F–S3H).

The only remaining immune cell types expressing CD40 that could be involved in $CD8^+$ T-cell activation were cDC2s (**Fig. 2B** and **C**). Importantly, it was previously shown that the transcriptional program

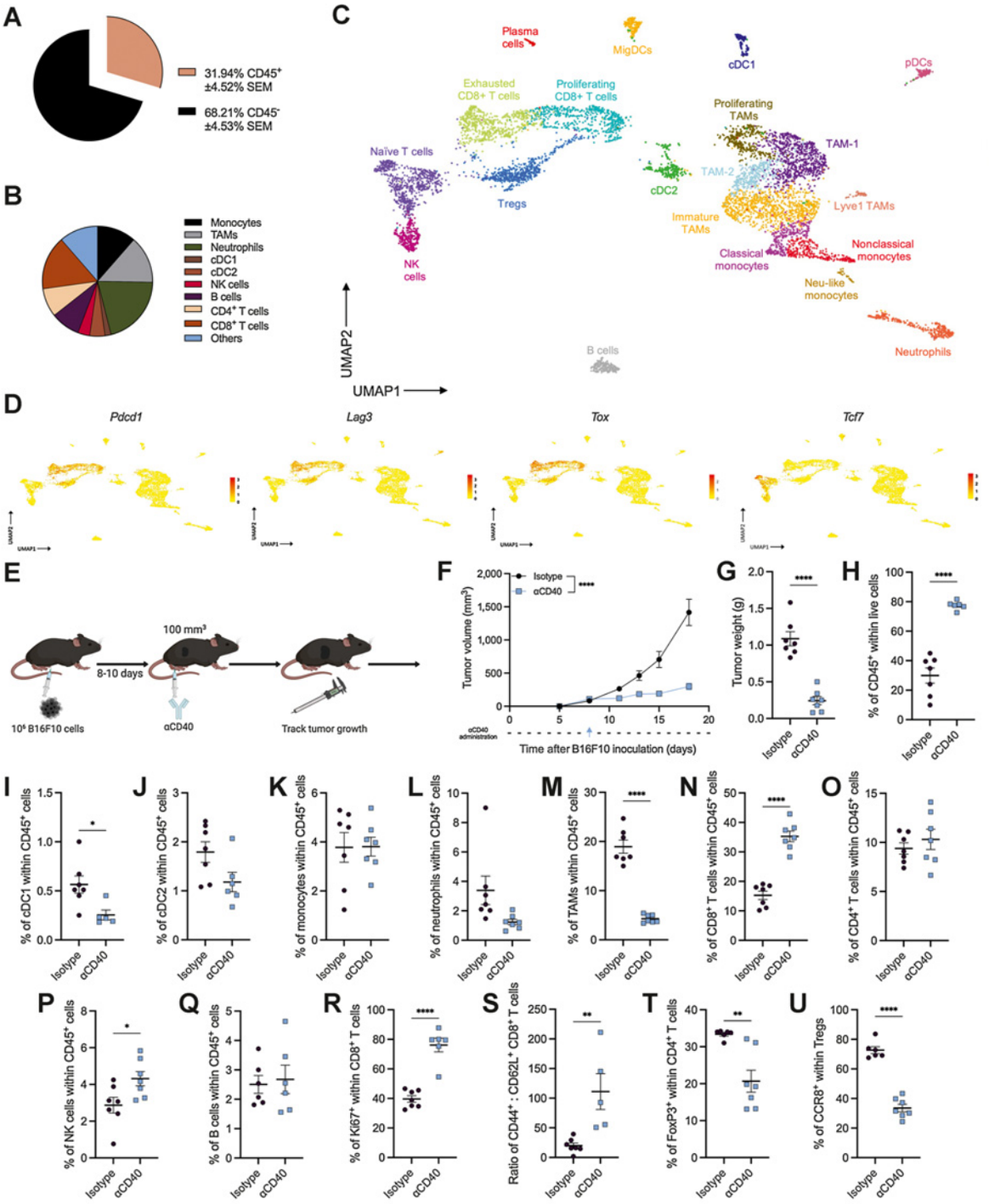

Figure 1.

CD40 agonist therapy slows the progression of B16F10 tumors. **A** and **B,** Pie charts representing the contribution of $CD45^+$ and $CD45^-$ cells in B16F10 tumors (**A**) and the distribution of different immune populations within the $CD45^+$ fraction (averages taken from 7 individual mice; **B**). **C** and **D,** UMAP plot of 6773 $CD45^+$ immune cells isolated from pools of three subcutaneous B16F10 tumors at a volume of ~1,055 ± 116.4 mm^3 (**C**) and expression of several key marker genes associated with $CD8^+$ T-cell function (**D**). **E–G,** Schematic representation (**E**) of the experimental setup indicating intraperitoneal αCD40 administration when tumors reach ≈100 mm^3 and the resulting effect of αCD40 administration on B16F10 tumor growth (**F**) and weight (**G**). **H,** Percentage of live cells that are $CD45^+$ within isotype and αCD40-treated B16F10 tumors. **I–Q,** Frequency of distinct immune populations within isotype or αCD40 treated B16F10 tumors. **R,** Percentage of $CD8^+$ T cells that express Ki67, required for cell proliferation. **S,** Ratio of $CD44^+$ $CD62L^-$ effector to $CD44^-$ $CD62L^+$ naïve tumor-infiltrating $CD8^+$ T cells. **T,** Percentage of $FoxP3^+$ cells within $CD4^+$ T cells in treated B16F10 tumors. **U,** Percentage of $CCR8^+$ Tregs within treated tumors. Representative data from three independent experiments ($n = 7$). *, $P < 0.05$; **, $P < 0.01$; ****, $P < 0.0001$.

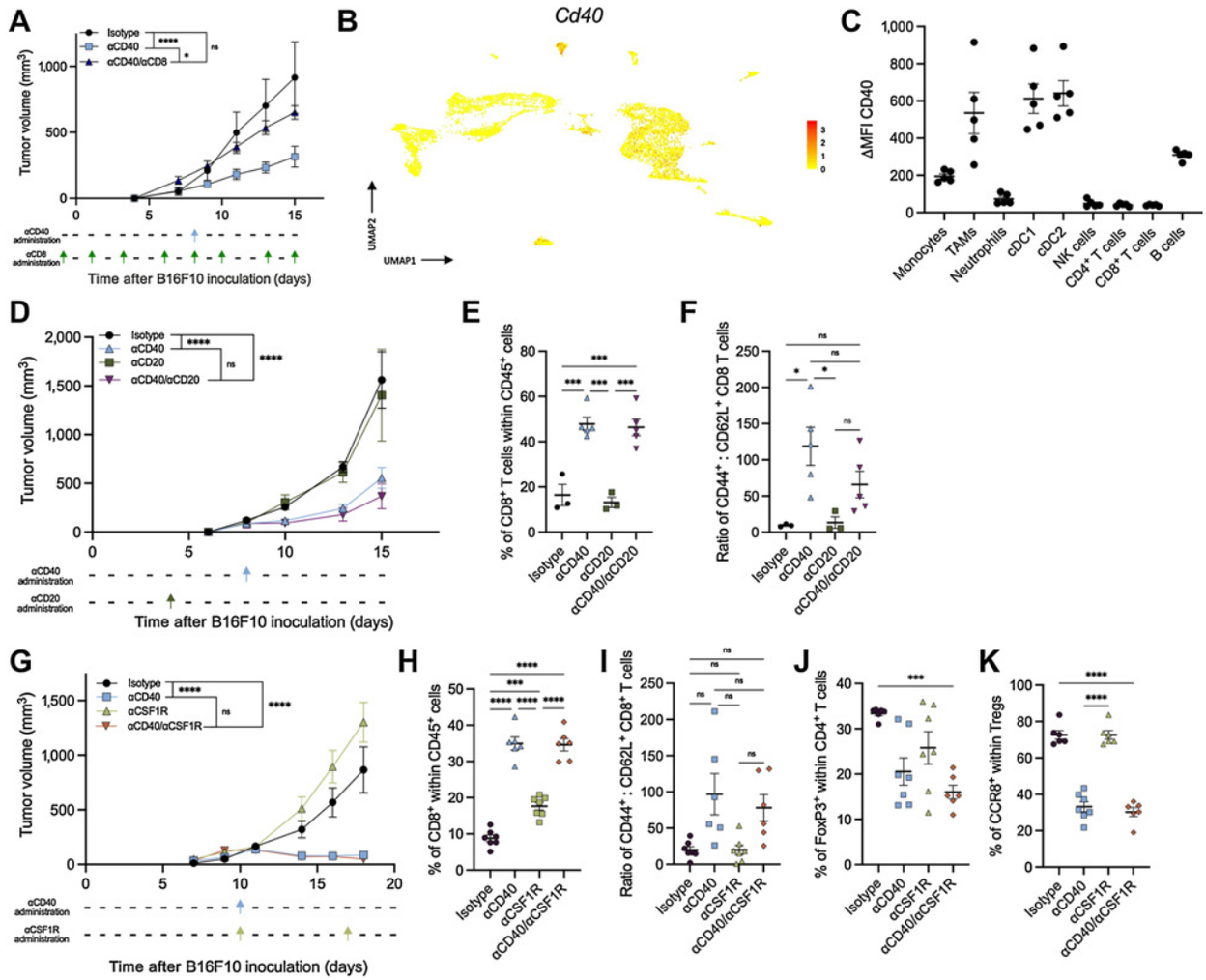

Figure 2.

αCD40 therapy in B16F10 is TAM and B-cell independent. **A,** Growth curve of B16F10 in WT mice after isotype, αCD40, or αCD40/αCD8 treatment. Data from one experiment ($n = 5$). **B,** UMAP showing *Cd40* mRNA expression within the CD45$^+$ fraction of B16F10 tumors with volume of 1,055 ±116.4 mm^3. **C,** CD40 protein expression across distinct CD45$^+$ cell subsets from 100 mm^3 B16F10 tumors, determined by the change in median fluorescence intensity (ΔMFI) of CD40 stained samples after subtraction of FMO background signal. Representative data from two independent experiments ($n = 5$). **D,** Growth curve of B16F10 in WT mice after isotype, αCD20, αCD40, or αCD20/αCD40 treatment. Representative data from two independent experiments ($n = 5$). **E** and **F,** Percentage (**E**) of and ratio of (**F**) CD44$^+$ CD62L$^-$ effector to CD44$^-$ CD62L$^+$ naïve CD8$^+$ T cells within B16F10 tumors after treatment. **G,** Growth curve of B16F10 in WT mice after isotype, αCD40, αCSF1R, or αCD40/αCSF1R treatment. Representative data from three independent experiments ($n = 7$). **H** and **I,** Percentage of (**H**) and ratio of (**I**) CD44$^+$ effector to CD62L$^+$ naïve CD8$^+$ T cells within B16F10 tumors after treatment. **J,** Percentage of FoxP3$^+$ cells within CD4$^+$ T cells infiltrating B16F10 tumors after treatment. **K,** Percentage of CCR8$^+$ Tregs within B16F10 tumors after treatment. ns, nonsignificant; *, $P < 0.05$; ***, $P < 0.001$; ****, $P < 0.0001$.

of cDC1s and cDC2s converged upon differentiation into MigDCs in various scRNA-seq analyses (43, 45). Two genes that showed specific upregulation in the MigDC cluster in our B16F10 data were *Ccr7* and *Cd200* (**Fig. 3H** and **I**; Supplementary Fig. S3I). After αCD40 administration, a higher proportion of both cDC1 and cDC2 expressed either receptor (**Fig. 3J–M**) and the frequency MigDCs, gated based on CD200 expression, was increased, whereas both cDC1 and cDC2 were reduced in frequency (Supplementary Figs. S3J–S3M). This is in line with the results we obtained when reanalyzing a publicly available scRNA-seq dataset of murine MC38-tumor bearing WT mice generated by Zhang and colleagues (32). Our analysis showed that the cDC1s and cDC2s were adopting a *Ccr7* expressing MigDC profile 48 hours after αCD40 treatment (Supplementary Figs. S3N–S3O). This might suggest that cDC2 activated by αCD40-agonist could adopt a MigDC transcriptional phenotype and mediate the activation of preexisting CD8$^+$ T-cell clones. Moreover, MHC-I levels on cDC2s were also increased upon αCD40 treatment (Supplementary Fig. S3P), further suggesting that as was shown in human (46, 47), cDC2s might be able to stimulate CD8$^+$ T cells.

DC-derived IL12 was previously shown to stimulate T-cell immunity (16). In B16F10 tumors, IL12 was mainly upregulated in the MigDC cluster, both at the transcript and protein level (**Fig. 3N**; Supplementary Fig. S3Q). To parse the role of cDC2/MigDC-derived IL12 in effective αCD40 therapy, we depleted cDC1s and TAMs and treated *Xcr1*$^{wt/dtr}$ mice with αCD40/αCSF1R while neutralizing IL12. Blockade of IL12 rendered the mice nonresponsive to αCD40 therapy

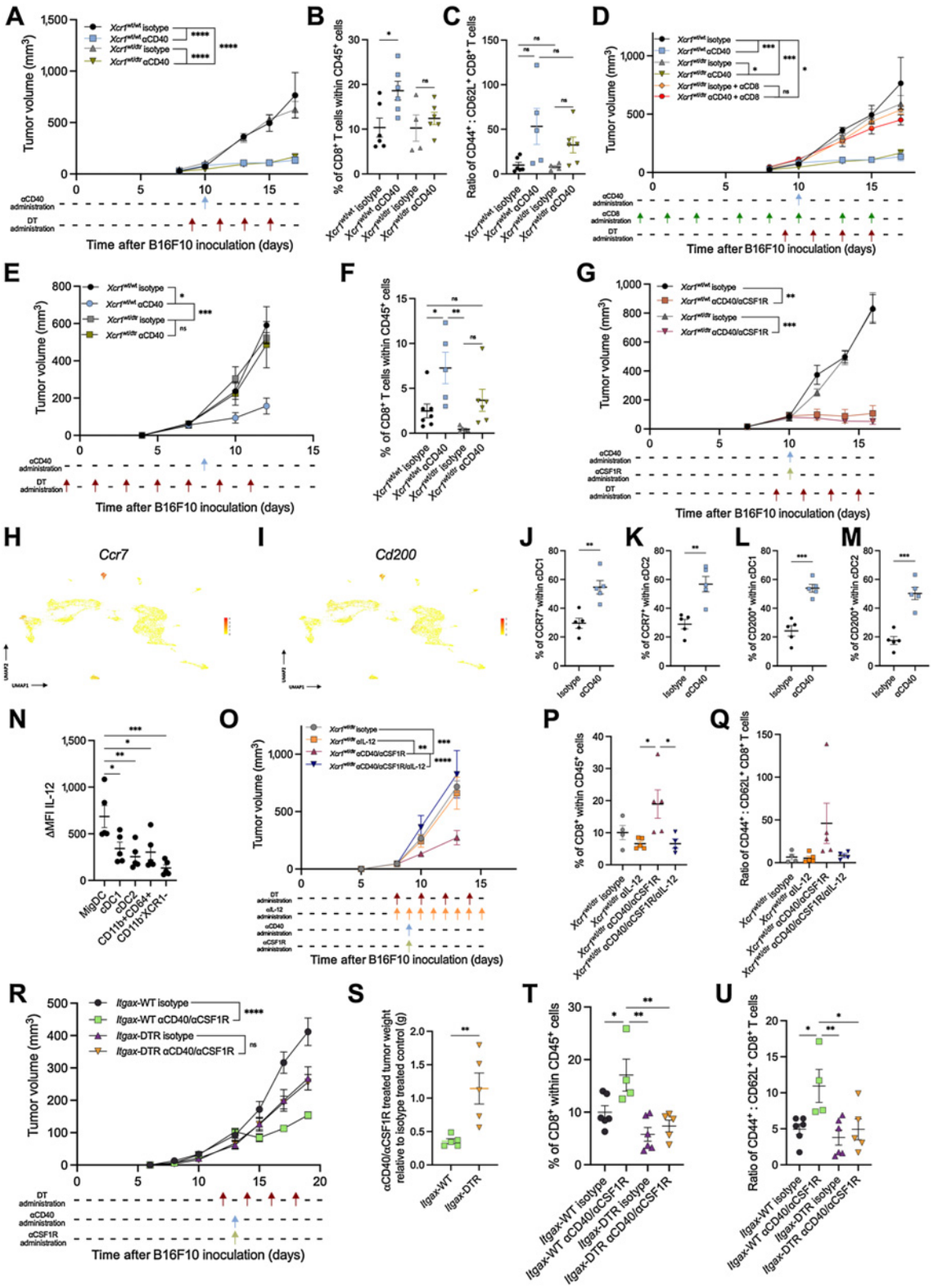
A
Tumor volume (mm3)
Xcr1wt/wt isotype
Xcr1wt/wt αCD40
Xcr1wt/dtr isotype
Xcr1wt/dtr αCD40
αCD40 administration
DT administration
Time after B16F10 inoculation (days)
B
% of CD8+ T cells within CD45+ cells
C
Ratio of CD44+ : CD62L+ CD8+ T cells
D
Tumor volume (mm3)
Xcr1wt/dtr isotype + αCD8
Xcr1wt/dtr αCD40 + αCD8
αCD8 administration
Time after B16F10 inoculation (days)
E
Tumor volume (mm3)
Time after B16F10 inoculation (days)
F
% of CD8+ T cells within CD45+ cells
G
Tumor volume (mm3)
Xcr1wt/wt αCD40/αCSF1R
Xcr1wt/dtr αCD40/αCSF1R
αCSF1R administration
Time after B16F10 inoculation (days)
H
Ccr7
I
Cd200
J
% of CCR7+ within cDC1
K
% of CCR7+ within cDC2
L
% of CD200+ within cDC1
M
% of CD200+ within cDC2
Isotype
αCD40
N
ΔMFI IL-12
MigDC
cDC1
cDC2
CD11b+CD64+
CD11b+XCR1-
O
Tumor volume (mm3)
Xcr1wt/dtr isotype
Xcr1wt/dtr αIL-12
Xcr1wt/dtr αCD40/αCSF1R
Xcr1wt/dtr αCD40/αCSF1R/αIL-12
DT administration
αIL-12 administration
αCD40 administration
αCSF1R administration
Time after B16F10 inoculation (days)
P
% of CD8+ within CD45+ cells
Xcr1wt/dtr isotype
Xcr1wt/dtr αIL-12
Xcr1wt/dtr αCD40/αCSF1R
Xcr1wt/dtr αCD40/αCSF1R/αIL-12
Q
Ratio of CD44+ : CD62L+ CD8+ T cells
R
Tumor volume (mm3)
Itgax-WT isotype
Itgax-WT αCD40/αCSF1R
Itgax-DTR isotype
Itgax-DTR αCD40/αCSF1R
DT administration
αCD40 administration
αCSF1R administration
Time after B16F10 inoculation (days)
S
αCD40/αCSF1R treated tumor weight relative to isotype treated control (g)
Itgax-WT
Itgax-DTR
T
% of CD8+ within CD45+ cells
Itgax-WT isotype
Itgax-WT αCD40/αCSF1R
Itgax-DTR isotype
Itgax-DTR αCD40/αCSF1R
U
Ratio of CD44+ : CD62L+ CD8+ T cells

and decreased the abundance and activation of tumor-infiltrating $CD8^+$ T cells compared with αCD40/αCSF1R-treated mice, demonstrating that IL12 was essential to the therapeutic efficacy of αCD40 in the absence of both cDC1s and TAMs (**Fig. 3O–Q**). Next, to investigate whether depleting all $CD11c^+$ cells (including cDC1, cDC2, and TAMs) within B16F10 tumors would abrogate the response to αCD40, we generated *Itgax*-DTR and *Itgax*-WT bone marrow chimeras to allow for continued depletion of $CD11c^+$ cells (Supplementary Figs. S3R–S3U). Interestingly, we found that upon depleting $CD11c^+$ cells, no differences were observed between isotype control and αCD40/αCSF1R treated mice, whereas tumor growth and the increase of effector $CD8^+$ T cells was still significantly reduced in WT reconstituted mice treated with αCD40/αCSF1R (**Fig. 3R–U**).

Overall, our data indicate that, although cDC1s play an important role in expanding $CD8^+$ T cells during early phases of tumor progression, they are dispensable for the activation of existing antitumor $CD8^+$ T-cell clones driving therapeutic αCD40 responses. On the other hand, our data suggest that cDC2s are capable of stimulating antitumor $CD8^+$ T cells in an IL12-dependent manner to reduce tumor growth upon CD40 agonist treatment.

TAM depletion can further delay tumor growth after αCD40 therapy in B16F10 tumors

Although αCD40 strongly reduced B16F10 tumor growth, long lasting antitumor responses were absent and eventually all mice lost tumor control approximately 5 days after the αCD40 treatment (**Fig. 4A**). Administration of a second dose of αCD40 5 days after the first dose did not provide any therapeutic benefit compared with mice that only received one αCD40 dose (**Fig. 4A**). When comparing the tumor immune infiltrate of the response phase on day 16 after tumor inoculation (tumor volume <400 mm^3) to the regrowth phase on day 21 after tumor inoculation (tumor volume >600 mm^3) upon αCD40 treatment, the myeloid compartment was more prominent in the latter at the expense of the $CD8^+$ T-cell infiltrate (**Fig. 4B**). Moreover, there was an enrichment of MMR^+ TAMs during the delayed regrowth phage, with MMR being a marker associated with a more protumor TAM phenotype (**Fig. 4C**). These data suggest that CD40 agonist therapy provides a short-term switch that polarizes the TME into an immunopermissive environment, but eventually the cytotoxic response subsides, resulting in therapy resistance and tumor regrowth.

Given that MMR^+ TAM have been shown to stimulate tumor relapse after therapy (48) and that in several preclinical tumor models αCD40/αCSF1R combination was able to reduce tumor growth synergistically (14, 15), we wondered whether TAMs would be contributing in the delayed regrowth after αCD40 treatment. Therefore, we treated mice with αCD40 + αCSF1R when tumors reached 100 mm^3. Indeed, TAM depletion on top of αCD40 treatment significantly delayed tumor growth (**Fig. 4D**), resulting in a prolonged survival compared with mice that received the αCD40 as monotherapy (**Fig. 4E**). The TME in αCD40 + αCSF1R-treated mice contained fewer TAMs compared with αCD40-monotherapy treated tumors (Supplementary Figs. S4A and S4B), from which the latter included fewer TAMs that expressed ARG1 and MMR (Supplementary Figs. S4C and S4D). Consequently, the abundance of $CD8^+$ T cells and their effector T-cell phenotype was increased in tumors of αCD40 + αCSF1R-treated mice (Supplementary Figs. S4E and S4F). Depletion of $CD8^+$ T cells 4 days after αCD40/αCSF1R administration prevented the protective effect generated by αCSF1R, showing that this effect was $CD8^+$ T-cell dependent (Supplementary Fig. S4G). These results indicate that although TAM depletion was not able to further improve the therapeutic effect of αCD40 during the response phase, αCSF1R treatment could prolong the antitumor responses to CD40 agonist therapy during the delayed regrowth phase.

B16F10 TAMs show a more immune stimulatory signature in comparison with LLC TAMs

Given the protumor role played by B16F10 TAMs upon αCD40 treatment during the delayed regrowth phase, we wondered whether the response to αCD40 would differ in preclinical models heavily infiltrated by TAMs during early tumor growth. Therefore, we utilized the LLC model, for which we previously showed the prominence of the myeloid compartment (40, 49). To investigate how the myeloid compartment differs between B16F10 and LLC tumors, we performed a scRNA-seq on the $CD45^+$ fraction of LLC tumors at similar tumor volumes as for the B16F10 scRNA-seq experiment (**Fig. 5A** and **B**; Supplementary Fig. S5A). Interestingly, the TME of LLC was characterized by a considerable heterogeneous myeloid infiltrate exemplified by expression of *Itgam*, whereas B16F10 tumors harbored more lymphocytes as indicated by expression of *Cd3e* (Supplementary Figs. S5B and S5C).

To explore the TAM heterogeneity between both models, we first subclustered the mononuclear populations, containing monocytes and TAMs and subsequently performed trajectory analysis. Some populations such as the monocyte, IFN-signature, and the two hypoxic TAM clusters were represented in both tumor models, whereas other TAM populations such as the TAM-1 and TAM-4 clusters appeared to be unique to B16F10 or LLC tumors, respectively (**Fig. 5C** and **D**). On the basis of differentially expressed (DE) genes between these clusters, we found that the TAMs, enriched in B16F10, expressed high levels of

Figure 3.

cDC1 function during early tumor growth determines αCD40 response. **A,** Growth curve of B16F10 in $Xcr1^{wt/wt}$ and $Xcr1^{wt/dtr}$ mice after isotype or αCD40 treatment with initial DT administration 24 hours prior to αCD40 administration. Representative data from two independent experiments ($n = 6$). **B** and **C,** Percentage of (**B**) and ratio of (**C**) $CD44^+$ effector to $CD62L^+$ naïve $CD8^+$ T cells infiltrating B16F10 tumors after treatment. **D,** Growth curve of B16F10 in $Xcr1^{wt/wt}$ and $Xcr1^{wt/dtr}$ mice after isotype, αCD40, αCD8, or αCD40/αCD8 treatment with initial DT administration 24 hours prior to αCD40. Representative data from two independent experiments ($n = 6$). **E,** Growth curve of B16F10 in $Xcr1^{wt/wt}$ and $Xcr1^{wt/dtr}$ mice after isotype or αCD40 treatment with initial DT administration 24 hours prior to B16F10 tumor implantation. Representative data from two independent experiments ($n = 6$). **F,** Percentage of $CD8^+$ T cells in B16F10 tumors after isotype of αCD40. **G,** Growth curve of B16F10 tumors in $Xcr1^{wt/wt}$ and $Xcr1^{wt/dtr}$ mice after isotype or αCD40/αCSF1R treatment, with initial DT administration 24 hours prior to αCD40. Data from one experiment ($n = 5$–9). **H** and **I,** UMAP plots of *Ccr7* (**H**) and *Cd200* (**I**) gene expression within $CD45^+$ fraction of ∼1,055 ±116.4 mm^3 B16F10 tumors. **J** and **K,** Percentage of $CCR7^+$ cDC1s (**J**) and cDC2s (**K**) within B16F10 tumors 24 hours after isotype or αCD40. **L** and **M,** Percentage of $CD200^+$ cDC1s (**L**) and cDC2s (**M**) within B16F10 tumors 24 hours after isotype or αCD40. **N,** Median fluorescence intensity quantification of IL12 expression in immune subsets including MigDC, cDC1, and cDC2 after subtraction of FMO signal 24 hours after isotype or αCD40. **O,** Growth curve of B16F10 tumors in $Xcr1^{wt/dtr}$ mice after treatment with isotype or αCD40/αCSF1R treatment with DT administration and IL12 neutralization beginning 24 hours prior to αCD40/αCSF1R treatment. Data from one experiment ($n = 5$–6). **P** and **Q,** Percentage of (**P**) and ratio of (**Q**) $CD44^+$ effector to $CD62L^+$ naïve tumor-infiltrating $CD8^+$ T cells after treatments. **R** and **S,** Growth curve (**R**) and weights (**S**) of B16F10 tumors in CD45.1 mice reconstituted with *Itgax*-WT and *Itgax*-DTR bone marrow after treatment with isotype or αCD40/αCSF1R, with initial DT administration 24 hours prior to αCD40/αCSF1R treatment. Data from one experiment ($n = 6$). **T** and **U,** Percentage of (**T**) and ratio of (**U**) $CD44^+$ effector to $CD62L^+$ naïve $CD8^+$ T cell in B16F10 tumors after treatment. ns, nonsignificant; *, $P < 0.05$; **, $P < 0.01$; ***, $P < 0.001$; ****, $P < 0.0001$.

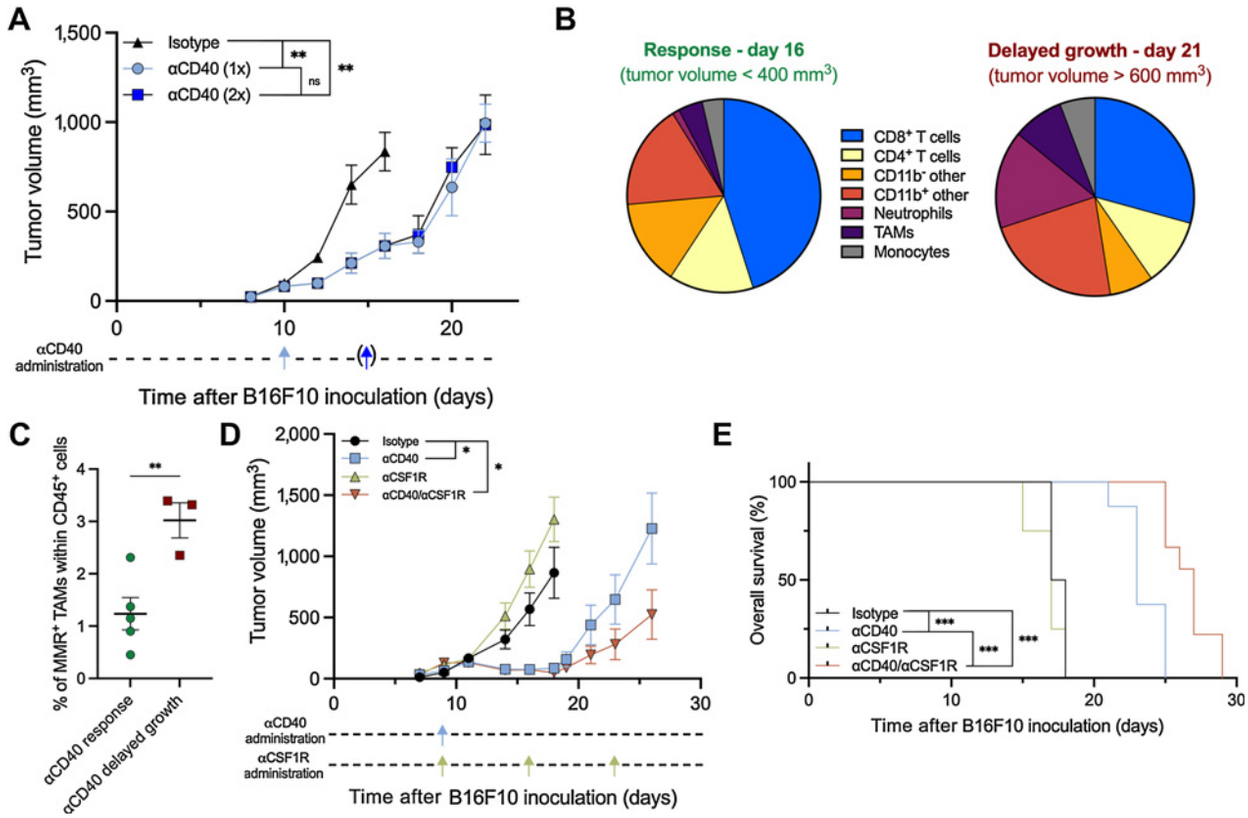

Figure 4.

αCSF1R prolongs survival of mice after delayed B16F10 tumor regrowth. **A,** Growth curve of B16F10 in WT mice after isotype, or αCD40 treatment. Data from one experiment ($n = 5$–15). **B,** Pie chart showing abundance of immune populations within B16F10 tumors during αCD40 response (day 16 after tumor inoculation, tumor volume ≈ 400 mm^3) and αCD40 regrowth (day 21 after tumor inoculation, tumor volume ≈ 600 mm^3; $n = 5$). **C,** Percentage of MMR$^+$ TAMs during αCD40 response and regrowth ($n = 3$–5). **D,** Growth curve of B16F10 tumors in WT mice after isotype, αCD40, αCSF1R, or αCD40/αCSF1R treatment. Representative data from two independent experiments ($n = 7$). **E,** Kaplan–Meier survival curve of B16F10 tumor-bearing mice after isotype, αCD40, αCSF1R, or αCD40/αCSF1R treatment, with death indicated as tumor volume >1,500 mm^3. Representative of two independent experiments ($n = 7$). ns, nonsignificant; *, $P < 0.05$; **, $P < 0.01$; ***, $P < 0.001$.

H2-DMb1, *Cxcl9*, and *Cxcl10*, which are associated with an MHC-II^{high} M1-like inflammatory TAM phenotype. The TAM clusters enriched in LLC expressed high levels of genes associated with anti-inflammation such as *Mrc1*, *Folr2*, and *Spp1* (**Fig. 5E–J**; Supplementary Figs. S5D and S5E). Interestingly, both LLC and B16F10 tumors harbored hypoxic TAM clusters expressing high levels of *Arg1*, *Vegfa*, *Bnip3*, and *Hildpa* (**Fig. 5K–N**; Supplementary Fig. S5F).

Trajectory inference using the Slingshot method predicted 3 distinct pseudotime lineages within TAMs (**Fig. 5O**). Lineage 1 was mainly represented by LLC TAMs, lineage 2 by B16F10 TAMs, and lineage 3, which contained the hypoxic TAMs, was shared by both models, indicating that the distinct monocyte-TAM lineages are tumor-type driven. Of note, cell percentages for each trajectory were calculated to correct for the fact that LLC tumors contained considerably more monocytes/TAMs (Supplementary Fig. S5G). Next, we performed gene ontology (GO) analysis on the DE genes at the end points of lineage 1 versus lineage 2 to further unravel the divergences between TAMs from B16F10 versus LLC tumors. For the genes specific for the LLC TAM trajectory, GO analysis highlighted besides "inflammatory response," terms related to cell adhesion, response to wound healing, angiogenesis, and negative regulation of cell population proliferation. In contrast, the GO terms "antigen processing and presentation," "positive regulation of T-cell activation," and "response to IFNγ" were highlighted for the B16F10 TAM trajectory (**Fig. 5P** and **Q**).

Overall, these results demonstrate that B16F10 tumors are enriched with lymphoid cells compared with LLC tumors and hint that monocyte to TAM differentiation and reprogramming is tumor-model specific with B16F10 TAMs developing toward T-cell stimulating cells, whereas LLC TAM develop towards potential wound-healing cells.

LLC tumors do not respond to αCD40 therapy when combined with TAM/neutrophil–depleting therapies nor therapies boosting CD8$^+$ T cells

On the basis of the inherent differences between the B16F10 and LLC TME, we wondered whether LLC could represent a model with an inherent resistance to αCD40 therapy. Indeed, treatment of LLC tumor-bearing mice with αCD40 as a monotherapy did not reduce tumor progression (**Fig. 6A** and **B**). Given the high protumor TAM infiltration into LLC tumors, we combined αCD40 with αCSF1R therapy. This resulted only in a small reduction in tumor growth, nonetheless, slightly repolarized the remaining TAM towards an MHC-II^{hi} phenotype and increased the neutrophil, CD4$^+$ and CD8$^+$ T-cell infiltrate, without altering the percentages of Tregs (**Fig. 6A–E**; Supplementary Figs. S6A–S6C).

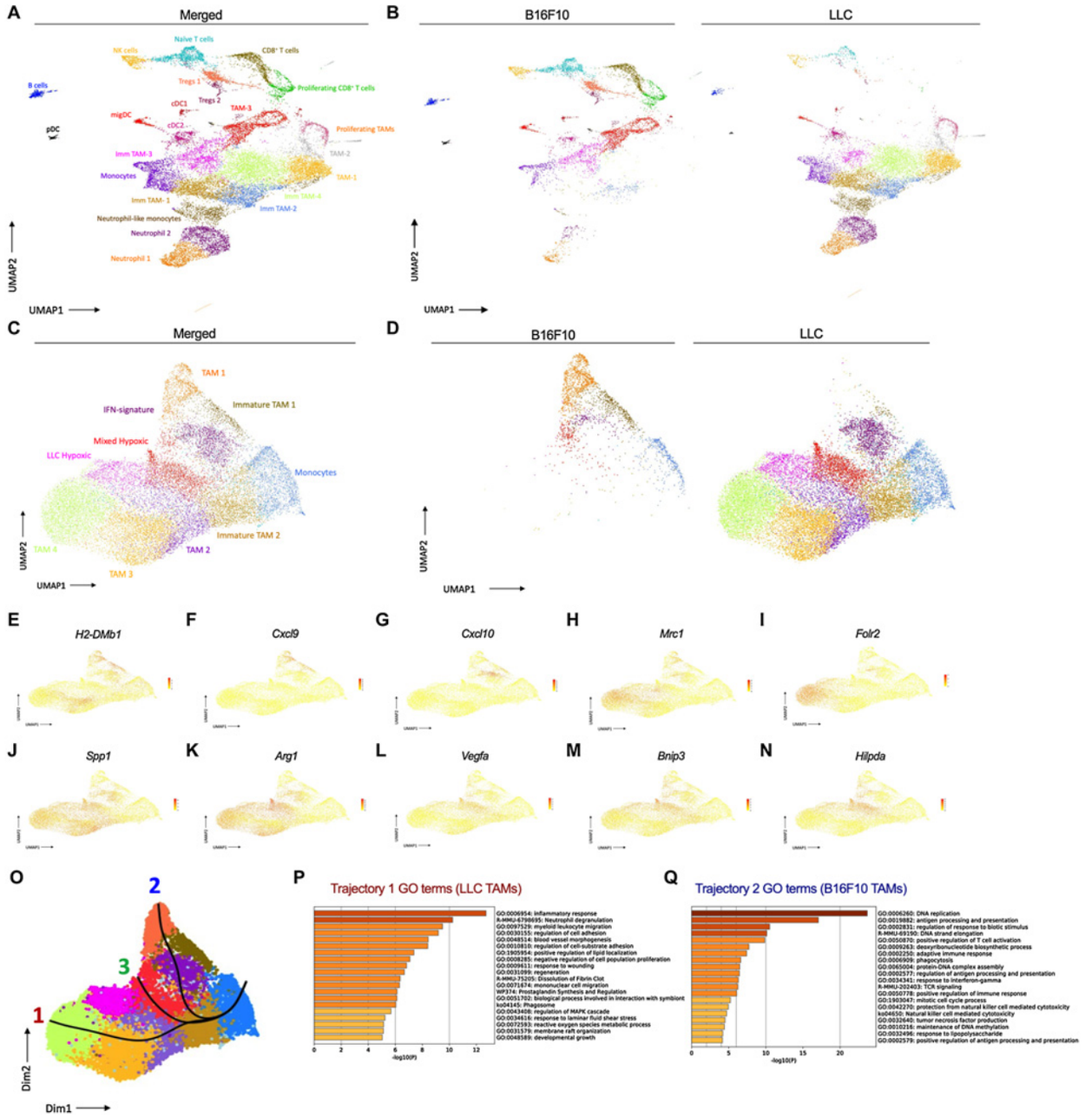

Figure 5.

Comparison of TAM subsets in B16F10 and LLC tumors show some conserved and tumor-specific gene signatures. **A,** UMAP plot of a merged dataset containing scRNA-seq and CITE-seq data from six individual LLC tumors (964.1 ±105.9 mm^3) and B16F10 tumor scRNA-seq data (1,055 ± 116.4 mm^3). **B,** UMAP plot of the merged dataset comparing the individually annotated $CD45^+$ cell populations between LLC and B16F10, split by tumor type. **C** and **D,** UMAP plots of the TAM and monocyte subset of the merged dataset (**C**) and separated by tumor type (**D**), containing 18,286 LLC cells and 2,297 B16F10 cells. **E–N,** UMAP plots showing key differentially expressed genes between the various subsets of B16F10 and LLC tumor-infiltrating monocytes and TAMs. **O,** Slingshot trajectory inference was run on the dataset containing B16F10 and LLC tumor-infiltrating monocytes and TAMs. Three distinct lineages were identified. **P** and **Q,** Top 20 enriched gene ontology terms from a gene ontology analysis of the genes enriched in the endpoint of lineage 1 (LLC TAMs) and lineage 2 (B16F10 TAMs; Wald statistic >100, log_2FC cutoff = 1.5 and −1.5, respectively).

We hypothesized that distinct immune players could be responsible for the resistance of LLC tumors towards αCD40 + αCSF1R therapy. When comparing B16F10 and LLC tumors, we observed a >4-fold increase in the abundance of tumor-infiltrating neutrophils in LLC (**Fig. 6F**). In addition, Tregs were strongly decreased upon αCD40 + αCSF1R treatment only in B16F10 (**Fig. 6G**). Both Tregs and neutrophils were shown to suppress $CD8^+$ T cells in LLC tumors (41, 49), which could be responsible for the lower initial abundance of $CD8^+$ T cells in LLC tumors and their inability to expand upon αCD40 + αCSF1R treatment (**Fig. 6H**).

First, to assess whether expanding the $CD8^+$ T-cell number in αCD40 + αCSF1R-treated LLC would result in a therapeutic response, we employed an optimized Flt3L treatment schedule to increase cDC numbers prior to therapy (Supplementary Figs. S6D and S6E). However, although this resulted in an increased $CD8^+$ T-cell abundance in αCD40 + αCSF1R-treated mice, tumor growth remained unaltered (**Fig. 6I–J**). Similarly, when depleting Tregs using an optimized αCD25 antibody regimen (Supplementary Fig. S6f), $CD8^+$ T cells were increased upon αCD40 + αCSF1R treatment but did not result in reduced tumor growth (**Fig. 6K** and **L**).

Finally, we addressed whether neutrophils would represent a resistance mechanism to αCD40 + αCSF1R therapy. Depletion of neutrophils pharmacologically in LLC tumors using αLy6G/αMAR regimens or CXCR2 inhibitors were unsuccessful when combined with αCSF1R (Supplementary Figs. S6G–S6J). To understand why neutrophils in LLC were not well depleted using CXCR2 inhibitors, we analyzed CXCR2 expression on neutrophils from bone marrow (BM), blood, spleen, and tumor in naïve or LLC tumor-bearing mice. We found that in both the naïve and tumor bearing scenario, approximately 50% of the neutrophils in the BM expressed CXCR2, a receptor required for neutrophil maturation and release from the BM (**Fig. 6M**; ref. 50). As expected, all neutrophils in blood and spleen expressed CXCR2, but surprisingly 50% of the neutrophils downregulated CXCR2 when reaching the TME. Interestingly, we saw that $CXCR2^+$ neutrophils suppressed T cells more compared with $CXCR2^-$ neutrophils (**Fig. 6N**). In αCD40 + αCSF1R-treated LLC-tumors, the $CXCR2^+$ neutrophil population was increased, emphasizing the therapeutic potential of neutrophil depletion in αCD40 + αCSF1R-treated mice (Supplementary Fig. S6K). However, unfortunately, when using *Csf3r*$^{-/-}$ mice, in which neutrophils are unable to egress from the BM, neutrophil depletion did not affect tumor growth of αCD40 + αCSF1R-treated mice (**Fig. 6O**; Supplementary Fig. S6L), implying that still other compensatory mechanisms are responsible for the therapy resistance of LLC tumors.

ICD-inducing therapy sensitizes LLC tumors to αCD40/αCSF1R therapy

Finally, we aimed to understand whether alternative complementary therapies could alleviate LLC tumor resistance and sensitize tumors to αCD40 + αCSF1R immunotherapy. Therefore, we inoculated mice with LLC cells expressing the chicken ovalbumin antigen as surrogate tumor antigen (LLC-OVA). In contrast to the results obtained in LLC, tumor growth was significantly reduced in LLC-OVA upon treatment with αCD40 and this response was even improved by the combination of αCD40 + αCSF1R, with the latter treated mice displaying prolonged survival (**Fig. 7A–C**). This antitumor effect was accompanied with a strong increase in $CD8^+$ T-cell abundance and a trend towards an increase in antigen-specific $CD8^+$ T cells, together with a repolarization of the remaining TAMs (**Fig. 7C–F**). Importantly, similar results were observed in mice bearing orthotopic LLC-OVA tumors. Micro-CT scanning revealed that the nonaerated lung volume and total lung volume, both parameters associated with lung tumor burden (35), were both reduced in mice treated with αCD40 + αCSF1R compared with mice treated with isotype, αCD40, or αCSF1R alone (Supplementary Figs. S7A–S7C). These results demonstrate that the presence of strong tumor antigens could resensitize resistant models to CD40 agonist therapy.

Next, we wanted to assess whether treating LLC tumors with ICD-inducing chemotherapy would recapitulate the results obtained in LLC-OVA tumors. ICD inducers have been reported to facilitate DC-based immunogenic phagocytosis of cell corpses, resulting in subsequent antigen specific T-cell activation (51). Hereto, we first evaluated which chemotherapies could induce most potent ICD in LLC. Oxaliplatin, generated the highest NF-κB and type I IFN responses in J774 macrophages cocultured with LLC cells (**Fig. 7G** and **H**). In LLC tumor-bearing mice treated with oxaliplatin, cancer cells indeed showed increased caspase-3 activity, indicative for an increased cancer cell death (**Fig. 7I**). Hence, to increase the rate of immunogenic LLC cell death, we combined αCD40 + αCSF1R with oxaliplatin. Oxaliplatin could significantly reduce LLC tumor progression when used in combination with αCD40 + αCSF1R and increased the proportions of $CD8^+$ T cells expressing an effector phenotype and granzyme B (**Fig. 7J–N**). Moreover, the remaining TAM were repolarized towards an MHC-II^{high} phenotype and less suppressive Tregs infiltrated tumors treated with the combination therapy (**Fig. 7O–R**). We found this antitumor effect to be mediated by the combination of the three therapies, as exclusion of αCSF1R resulted in the loss of antitumor immunity (Supplementary Fig. S7D–S7J). Interestingly, when depleting cDC1 using *Xcr1*$^{wt/dtr}$ mice during the αCD40 therapeutic window in LLC, we observed reduced sensitivity to the therapy and reduced $CD8^+$ T-cell numbers, highlighting the important role cDC1 play in antitumor $CD8^+$ T-cell responses in this model (Supplementary Figs. S7K–S7P). The therapeutic effect of the triple therapy was also recapitulated in orthotopic LLC tumors. Mice that had received oxaliplatin + αCD40 + αCSF1R had lower nonaerated lung volume, a proxy for the tumor burden, compared with all other groups (Supplementary Figs. S7Q–S7S).

Overall, these findings show that ICD-inducing chemotherapy could subvert αCD40 + αCSF1R therapy resistance and thereby resensitize resistant tumor models.

Discussion

Cancer therapies that aim to activate a patient's own immune cells hold a great deal of clinical promise. However, due to the potential to generate extreme adverse events, clinical application of agonist therapies must be performed with caution (52). In the case of CD40 agonists, MTDs have been identified and their clinical use appears safe for patients with solid tumors (53). To optimize CD40 agonist outcome, context-dependent cellular inputs are required for efficacy needs to be identified, as successful αCD40 therapy has been shown to rely on multiple cell types (14, 18, 23). Finally, investigation of appropriate combinatory approaches will ensure that a highest possible proportion of patients can potentially benefit from αCD40 agonist therapy.

In B16F10 tumors, the involvement of $CD8^+$ T cells and cDC1s was essential to generate CD40-mediated therapeutic responses. This is in accordance with previous findings that showed, using *Batf3* KO mice, that αCD40-mediated responses rely on the cDC1-$CD8^+$ T-cell axis in pancreatic ductal adenocarcinoma and bladder cancer (18, 54). However, *Batf3* KO mice have two potential drawbacks. First, they genetically lack critical cDC1 functions throughout all stages of tumor progression, making it challenging to evaluate cDC1 contribution in a temporal manner. Second, BATF3 input has been shown recently to be critical for memory $CD8^+$ T-cell development, indicating that these mice may also have intrinsic issues in memory $CD8^+$ T-cell formation, regardless of their dysfunctional cDC1 pool (55).

Surprisingly, using *Xcr1*$^{wt/dtr}$ mice, we observed that cDC1 function was only essential prior to αCD40 administration in the responsive B16F10 model, and that cDC1 were redundant during the actual therapeutic phase of αCD40.

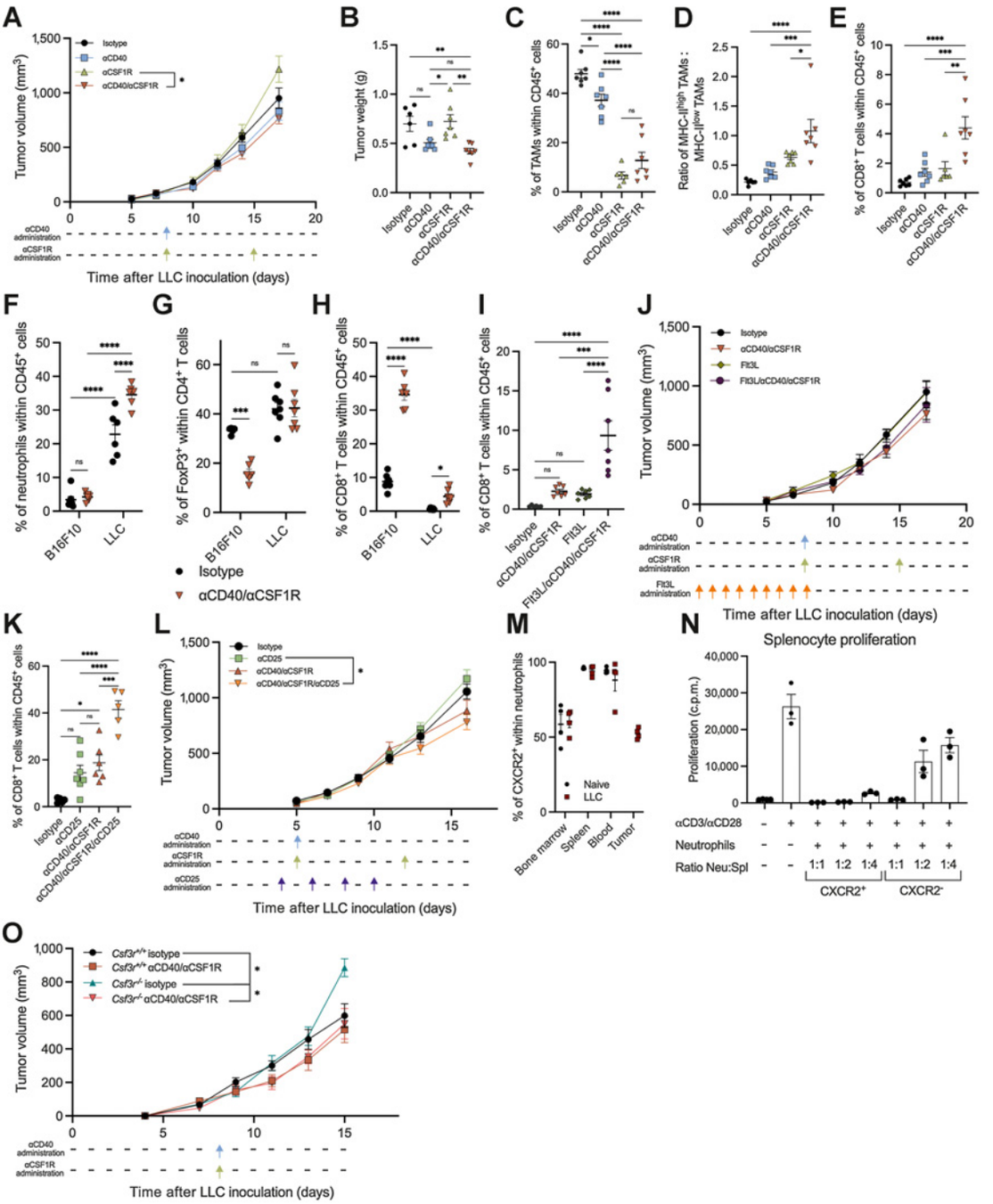

Figure 6.

Increasing CD8$^+$ T-cell infiltration into LLC tumors does not correlate with improved antitumor effects. **A** and **B,** Growth curve (**A**) and tumor weights (**B**) of LLC tumors in WT mice after isotype, αCD40, αCSF1R, and αCD40/αCSF1R treatment. Representative data from three independent experiments ($n = 7$). **C–E,** Percentage of TAMs (**C**), ratio of MHC-II^{high} to MHC-II^{low} TAMs (**D**), and percentage of CD8$^+$ T cells (**E**) within LLC tumors after treatment. **F–H,** Percentage of neutrophils (**F**), Tregs (**G**), and CD8$^+$ T cells (**H**) within LLC and B16F10 tumors after isotype or αCD40/αCSF1R treatment. **I,** Percentage of CD8$^+$ T cells within LLC tumors after Flt3L pretreatment and subsequent isotype or αCD40/αCSF1R treatment. Data from one experiment ($n = 7$). **J,** Growth curve of LLC tumors in WT mice after treatment with isotype, αCD40/αCSF1R, Flt3L, or Flt3L/αCD40/αCSF1R. Data from one experiment ($n = 7$). **K,** Percentage of CD8$^+$ T cells within LLC tumors after isotype, αCD25, αCD40/αCSF1R, or αCD40/αCSF1R/αCD25 treatment. Data from one experiment ($n = 7$). **L,** Growth curve of LLC tumors after isotype, αCD25, αCD40/αCSF1R, or αCD40/αCSF1R/αCD25 treatment. **M,** CXCR2 expression by neutrophils in bone marrow, spleen, blood, and tumor from naïve or LLC tumor-bearing mice. **N,** Splenocyte proliferation after coculture of splenocytes with day 15 LLC-derived CXCR2$^+$ or CXCR2$^-$ neutrophils measured via 3H-thymidine incorporation (c.p.m., count per minute; $n = 3$, data pooled from three independent experiments). **O,** Growth curve of LLC tumors in *Csf3r*$^{+/+}$ or *Csf3r*$^{-/-}$ after isotype or αCD40/αCSF1R treatment. Representative data from two independent experiments ($n = 7$). ns, nonsignificant; *, $P < 0.05$; **, $P < 0.01$; ***, $P < 0.001$; ****, $P < 0.0001$.

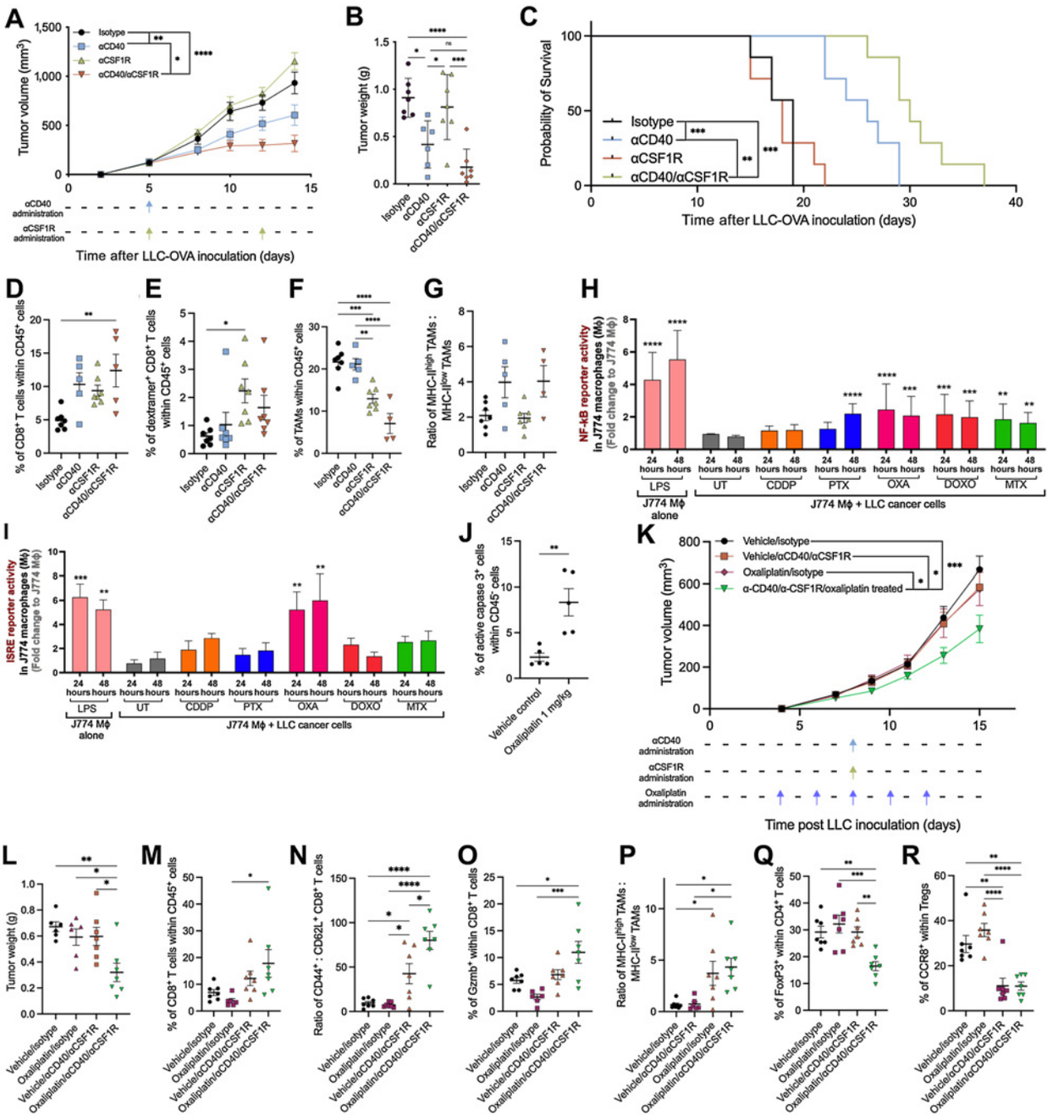

Figure 7.

Oxaliplatin synergizes with αCD40/αCSF1R therapy in LLC. **A** and **B,** Growth curve of LLC-OVA tumors (**A**) and tumor weights (**B**) from WT mice after isotype, αCD40, αCSF1R, or αCD40/αCSF1R treatment. Representative data from three independent experiments ($n = 7$). **C,** Kaplan–Meier survival curve of LLC-OVA tumor-bearing mice after isotype, αCD40, αCSF1R, or αCD40/αCSF1R treatment, with death indicated as tumor volume >1,500 mm^3. Data from one experiment ($n = 7$). **D,** Infiltration of $CD8^+$ T cells into LLC-OVA tumors after isotype, αCD40, αCSF1R, or αCD40/αCSF1R treatment. **E,** Percentage of $dextramer^+$ $CD8^+$ T cells within LLC-OVA tumors after treatment. **F** and **G,** Infiltration of TAMs into LLC-OVA tumors (**F**) and the ratio of intratumoral MHC-II^{high} to MHC-II^{low} TAMs (**G**). **H** and **I,** NF-κB (**H**) or ISRE (**I**) reporter activity in J774 macrophages cell 24 and 48 hours after culturing with LPS alone, or coculturing with LLC cancer cells and subsequent addition of indicated chemotherapeutic compounds ($n = 3$). **J,** Percentage of live $CD45^-$ cells within LLC tumors after treatment with vehicle or oxaliplatin. Representative data from two independent experiments ($n = 5$). **K** and **L,** Growth curve of LLC tumors (**K**) and tumor weights (**L**) after treatment with vehicle or oxaliplatin and isotype or αCD40/αCSF1R antibodies. Representative data from two independent experiments ($n = 7$). **M,** Percentage of $CD8^+$ T cells infiltrating LLC tumors after treatment. **N,** Ratio of $CD44^+$ effector to $CD62L^+$ naïve tumor-infiltrating $CD8^+$ T cells. **O,** Percentage of LLC tumor-infiltrating granzyme B^+ $CD8^+$ T cells. **P,** Ratio of MHC-II^{high} to MHC-II^{low} TAMs within LLC tumors after treatment. **Q,** Percentage of $FoxP3^+$ cells within $CD4^+$ T cells infiltrating LLC tumors after treatment. **R,** Percentage of $CCR8^+$ Tregs within LLC tumors after treatment. ns, nonsignificant; *, $P < 0.05$; **, $P < 0.01$; ***, $P < 0.001$; ****, $P < 0.0001$.

Strikingly, during the later stages of tumor progression, we showed that another cell type, likely cDC2s that upon αCD40-activation adopt a MigDC phenotype, was able to activate $CD8^+$ T cells in the absence of cDC1 and TAMs. A transcriptional heterogeneity of cDC2s within mice was demonstrated in multiple cancer types, with similar counterparts also being identified in human cancers (56). Moreover, a population of inflammatory $CD64^+$ cDC2s, capable of priming both $CD4^+$ and $CD8^+$ T cells within a respiratory viral infection setting were recently identified (57), suggesting that cDC1s are not the only cell types able to cross present antigens to $CD8^+$ T cells. As such, in the cancer context, human circulating inflammatory $CD88^-CD1c^+CD163^+$ DCs were shown to regulate tumor immunity (58) and human cDC2s were proposed as critical mediators of cross-presentation of tumor antigens thereby promoting potent antitumor CTL responses (46, 47). Curiously, despite their different functional specializations, both cDC1 and cDC2 adopt an overlapping transcriptional signature upon activation and differentiation to MigDCs (27, 43, 45). Whether the ontogeny-related functions of cDC1 or cDC2 persist despite the altered signature has yet to be proven, although as cDC2 and cDC2-derived MigDCs are not depleted in *Xcr1*$^{wt/dtr}$ mice, our data strongly suggest that these cells could be responsible for $CD8^+$ T-cell activation in response to αCD40 therapy. As such, although the presence and function of intratumoral cDC1s has been shown an important player for the success of αCD40 therapy, the antitumor functions performed by cDC2s in response to CD40 agonist therapy can be more important than initially thought.

In response to CD40 agonist therapy, B16F10 tumor growth was controlled for multiple days. However, all mice would eventually lose tumor control and display a delayed tumor regrowth occurrence. Similar observations have been made using a combination of CD40L, TNFα, and an antibody against the melanoma antigen TRP1 in which the B16F10 cancer cells formed cell-in-cell structures to avoid immune recognition (59). This process was suggested to be mediated by IFNγ-activated $CD8^+$ T cells, and once T cells were no longer present, the cancer cells would disassociate from one another and continue growing. Interestingly, when we depleted TAMs, we observed a higher proportion of $CD8^+$ T cells associated with prolonged survival and delayed tumor regrowth. This could suggest that the presence of $CD8^+$ T-cell suppressive TAM could be associated with a faster disruption of the $CD8^+$ T-cell-mediated cell-in-cell structures and subsequent tumor regrowth.

Because of their plasticity, TAMs represent an important therapeutic target. CD40 therapy has also been shown to rely on the presence and subsequent repolarization of TAMs to generate antitumor immunity (14, 23). The effect of αCD40 therapy on primary tumor growth was not enhanced with TAM depletion in the B16F10 model, yet TAM might have undergone a rapid reprogramming in response to CD40 agonist before their depletion as was shown in other models (14). Interestingly, when merging scRNA-seq data of untreated B16F10 TAMs and TAMs from the heavily infiltrated LLC model, we found considerable tumor-specific heterogeneity and polarization. B16F10 TAMs appeared to be more immune-stimulatory compared with LLC TAMs. Nevertheless, when B16F10 tumors started to regrow, TAMs adopted a MMR^+ protumor phenotype, at which point the net depletion of TAMs had a beneficial effect on survival. These results hint that a more nuanced approach to TAM depletion may result in better antitumor effects, as broad depletion using αCSF1R may also deplete antitumor TAM populations (32, 49), although more antitumoral TAMs have been shown to rely less on CSF1R for their survival (60).

Finally, with regard to the clinical application of CD40 agonists, our data suggest that different tumor types would benefit from different combinations of therapies. While stimulating $CD8^+$ T-cell responses against tumors is a critical facet of any successful immunotherapy, our results indicate that an underlying $CD8^+$ T-cell response must exist in order for αCD40 to function as a monotherapy. Therefore, if patient stratification occurs based on tumor CD3 complexity, further assessment should be made to determine whether the T cells present can recognize relevant tumor antigens or not since the intratumoral $CD8^+$ T-cell pool has been shown to contain considerable irrelevant $CD8^+$ T cells (61, 62). Patients with immune desert tumors would require more nuanced combination therapies, such as chemotherapy or radiotherapy, that would aim to generate an antitumor immune response that could be amplified with αCD40 therapy (20, 25, 26). Although CD40 agonists have achieved beneficial clinical outcomes in pancreatic cancer when combined with chemotherapy (20), the potential for toxicity remains a major caveat limiting their use (53, 63, 64). Encouragingly, although we suggest DCs as one of the critical mediators of antitumor immunity in response to αCD40, DCs have recently been shown to not be involved in αCD40-associated toxicity (65), suggesting that another layer of potential therapeutic combinations exist that could offset tissue damage while preserving the antitumor function of αCD40.

Authors' Disclosures

A. Murgaski reports grants from Fonds Wetenschappelijk Onderzoek (FWO) and Kom op tegen Kanker (KOTK) during the conduct of the study. E. Hadadi reports grants from Research Foundation Flanders (FWO) during the conduct of the study. S. Hoves reports a patent 20200392234 pending, a patent 20190284284 pending, a patent 20180346581 pending, a patent 20170051065 pending, a patent 20160220669 pending, a patent 9192667 issued, a patent 20150073129 pending, and a patent 20140314771 pending; and also reports employment with Roche Diagnostics GmbH and ownership of Hoffmann La Roche stock. S. Deschoemaeker reports grants from Stichting tegen Kanker post-doctoraal mandaat (2021-023) during the conduct of the study. M. Schmittnaegel reports employment with Roche Diagnostics GmbH. C.H. Ries reports personal fees from Roche during the conduct of the study; personal fees from Macomics Ltd. and Dr. Carola Ries Consulting outside the submitted work; also has a patent for EP12158519 issued. D. Laoui reports other support from Roche and grants from FWO, VUB, and Collen-Francqui Foundation during the conduct of the study. No disclosures were reported by the other authors.

Authors' Contributions

A. Murgaski: Conceptualization, data curation, formal analysis, validation, investigation, visualization, methodology, writing–original draft, project administration, writing–review and editing. **M. Kiss:** Conceptualization, investigation, writing–review and editing. **H. Van Damme:** Investigation, writing–review and editing. **D. Kancheva:** Data curation, software, formal analysis, visualization, methodology, writing–review and editing. **I. Vanmeerbeek:** Data curation, formal analysis, validation, investigation, visualization, methodology. **J. Keirsse:** Investigation. **E. Hadadi:** Investigation, writing–review and editing. **J. Brughmans:** Investigation. **S.M. Arnouk:** Investigation. **A.E. Hamouda:** Investigation. **A. Debraekeleer:** Investigation. **V. Bosteels:** Resources, investigation, methodology, writing–review and editing. **Y. Elkrim:** Investigation. **L. Boon:** Resources. **S. Hoves:** Resources, writing–review and editing. **N. Vandamme:** Resources, data curation, software, investigation, methodology. **S. Deschoemaeker:** Resources, investigation, writing–review and editing. **S. Janssens:** Resources, methodology, writing–review and editing. **A.D. Garg:** Data curation, formal analysis, validation, investigation, visualization, methodology, writing–review and editing. **G. Vande Velde:** Investigation, methodology. **M. Schmittnaegel:** Resources, writing–review and editing. **C.H. Ries:** Resources. **D. Laoui:** Conceptualization, resources, data curation, supervision, funding acquisition, writing–review and editing.

Acknowledgments

The authors thank Kasia Błażejczyk, Ella Omasta, Marie-Therese Detobel, Nickey Van Riebeek, Nadia Abou, and Christopher Stanley for technical assistance and administrative

assistance. They thank Pascal Merchiers, Akiko Iwasaki, and Orr-El Weizman for providing reagents. The authors thank the VIB singularity platform for support and access to scRNA-seq technologies and Ria Roelandt for the library preparations. They thank Mikaël Pittet, Patrick De Baetselier, Jo Van Ginderachter, and Kiavash Movahedi for insightful discussions. A. Murgaski, H. Van Damme, I. Vanmeerbeek, and S.M. Arnouk are supported by an FWO doctoral fellowship (1S16718N, 1S24117N, 1S06821N, and 1S78120N). S. Janssens and V. Bosteels are funded by an EOS grant (G0G7318N) and FWO predoctoral fellowship. A.D. Garg was supported by FWO (G0B4620N; EOS grant 30837538), KU Leuven, Kom op Tegen Kanker, and VLIR-UOS. G. Vande Velde was supported by KU Leuven Internal Funds (C24/17/061 and STG/15/024). D. Laoui was supported by grants from FWO (12Z1820N), Kom op Tegen Kanker, Stichting tegen kanker, and Vrije Universiteit Brussel.

The publication costs of this article were defrayed in part by the payment of publication fees. Therefore, and solely to indicate this fact, this article is hereby marked "advertisement" in accordance with 18 USC section 1734.

Note

Supplementary data for this article are available at Cancer Research Online (http://cancerres.aacrjournals.org/).

Received January 13, 2022; revised June 23, 2022; accepted August 1, 2022; published first August 18, 2022.

References

1. Jemal A, Ward EM, Johnson CJ, Cronin KA, Ma J, Ryerson AB, et al. Annual report to the nation on the status of cancer, 1975–2014, featuring survival [Internet]. J Natl Cancer Inst; 2017. https://academic.oup.com/jnci/article/109/9/djx030/3092246.
2. Hegde PS, Chen DS. Top 10 challenges in cancer immunotherapy. Immunity 2020;52:17–35.
3. Sharma P, Siddiqui BA, Anandhan S, Yadav SS, Subudhi SK, Gao J, et al. The next decade of immune checkpoint therapy. Cancer Discov 2021;11:838–57.
4. Vonderheide RH. CD40 agonist antibodies in cancer immunotherapy. Annu Rev Med 2020;71:1–12.
5. Ridge JP, Di Rosa F, Matzinger P. A conditioned dendritic cell can be a temporal bridge between a CD4 + T-helper and a T-killer cell. Nature 1998;393:474–8. https://pubmed.ncbi.nlm.nih.gov/9624003/.
6. Bennett SRM, Carbone FR, Karamalis F, Flavell RA, Miller JFAP, Heath WR. Help for cytotoxic-T-cell responses is mediated by CD4O signalling. Nature 1998;393:478–80. https://pubmed.ncbi.nlm.nih.gov/9624004/.
7. Schoenberger SP, Toes REM, Van Dervoort EIH, Offringa R, Melief CJM. T-cell help for cytotoxic T lymphocytes is mediated by CD40-CD4OL interactions. Nature 1998;393:480–3. https://pubmed.ncbi.nlm.nih.gov/9624005/.
8. Van Kooten G, Banchereau J. CD40-CD40 ligand. J Leukoc Biol 2000;67:2–17. https://pubmed.ncbi.nlm.nih.gov/10647992/.
9. Van Mierlo GJD, BAT Den, Medema JP, Van Der Voort EIH, Fransen MF, Offringa R, et al. CD40 stimulation leads to effective therapy of CD40- tumors through induction of strong systemic cytotoxic T lymphocyte immunity. Proc Natl Acad Sci U S A 2002;99:5561–6. https://pubmed.ncbi.nlm.nih.gov/11929985/.
10. Mangsbo SM, Broos S, Fletcher E, Veitonmäki N, Furebring C, Dahlén E, et al. The human agonistic CD40 antibody ADC-1013 eradicates bladder tumors and generates T-cell-dependent tumor immunity. Clin Cancer Res 2015;21:1115–26. http://clincancerres.aacrjournals.org/.
11. Vonderheide RH, Flaherty KT, Khalil M, Stumacher MS, Bajor DL, Hutnick NA, et al. Clinical activity and immune modulation in cancer patients treated with CP-870,893, a novel CD40 agonist monoclonal antibody. J Clin Oncol 2007;25:876–83. https://pubmed.ncbi.nlm.nih.gov/17327609/.
12. Kashyap AS, Schmittnaegel M, Rigamonti N, Pais-Ferreira D, Mueller P, Buchi M, et al. Optimized antiangiogenic reprogramming of the tumor microenvironment potentiates CD40 immunotherapy. Proc Natl Acad Sci U S A 2020;117:541–51.
13. Wiehagen KR, Girgis NM, Yamada DH, Smith AA, Chan SR, Grewal IS, et al. Combination of CD40 agonism and CSF-1R blockade reconditions tumor-associated macrophages and drives potent antitumor immunity. Cancer Immunol Res 2017;5:1109–21. http://cancerimmunolres.aacrjournals.org/lookup/doi/10.1158/2326–6066.CIR-17–0258.
14. Hoves S, Ooi C-H, Wolter C, Sade H, Bissinger S, Schmittnaegel M, et al. Rapid activation of tumor-associated macrophages boosts preexisting tumor immunity. J Exp Med 2018;jem.20171440. http://www.jem.org/lookup/doi/10.1084/jem.20171440.
15. Perry CJ, Muñoz-Rojas AR, Meeth KM, Kellman LN, Amezquita RA, Thakral D, et al. Myeloid-targeted immunotherapies act in synergy to induce inflammation and antitumor immunity. J Exp Med 2018;215:877–93. http://www.jem.org/lookup/doi/10.1084/jem.20171435.
16. Garris CS, Arlauckas SP, Kohler RH, Trefny MP, Garren S, Piot C, et al. Successful anti-PD-1 cancer immunotherapy requires T cell-dendritic cell crosstalk involving the cytokines IFN-γ and IL-12. Immunity 2018;49:1148–61. http://www.ncbi.nlm.nih.gov/pubmed/30552023.
17. Ngiow SF, Young A, Blake SJ, Hill GR, Yagita H, Teng MWL, et al. Agonistic CD40 mAb-driven IL12 reverses resistance to anti-PD1 in a T-cell-rich tumor. Cancer Res 2016;76:6266–77.
18. Byrne KT, Vonderheide RH. CD40 stimulation obviates innate sensors and drives T cell immunity in cancer. Cell Rep 2016;15:2719–32. https://www.ncbi.nlm.nih.gov/pmc/articles/PMC4917417/pdf/nihms789643.pdf.
19. Rech AJ, Dada H, Kotzin JJ, Henao-Mejia J, Minn AJ, Victor CT-S, et al. Radiotherapy and CD40 activation separately augment immunity to checkpoint blockade in cancer. Physiol Behav 2017;176:139–48.
20. O'Hara MH, O'Reilly EM, Varadhachary G, Wolff RA, Wainberg ZA, Ko AH, et al. CD40 agonistic monoclonal antibody APX005M (sotigalimab) and chemotherapy, with or without nivolumab, for the treatment of metastatic pancreatic adenocarcinoma: an open-label, multicentre, phase 1b study. Lancet Oncol 2021;22:118–31.
21. Böttcher JP, Reis e Sousa C. The role of type 1 conventional dendritic cells in cancer immunity. Trends Cancer 2018;4:784–92. https://doi.org/10.1016/j.trecan.2018.09.001.
22. Broz ML, Binnewies M, Boldajipour B, Nelson AE, Pollack JL, Erle DJ, et al. Dissecting the tumor myeloid compartment reveals rare activating antigen-presenting cells critical for T cell immunity. Cancer Cell 2014;26:638–52. https://linkinghub.elsevier.com/retrieve/pii/S1535610814003705.
23. Beatty GL, Chiorean EG, Fishman MP, Saboury B, Teitelbaum UR, Sun W, et al. CD40 agonists alter tumor stroma and show efficacy against pancreatic carcinoma in mice and humans. Science 2011;331:1612–6. https://pubmed.ncbi.nlm.nih.gov/21436454/.
24. Schetters STT, Rodriguez E, Kruijssen LJW, Crommentuijn MHW, Boon L, Van Den Bossche J, et al. Monocyte-derived APCs are central to the response of PD1 checkpoint blockade and provide a therapeutic target for combination therapy. J Immunother Cancer 2020;8:1–16.
25. Hegde S, Krisnawan VE, Herzog BH, Zuo C, Breden MA, Knolhoff BL, et al. Dendritic cell paucity leads to dysfunctional immune surveillance in pancreatic cancer. Cancer Cell 2020;37:289–307.
26. Lin JH, Huffman AP, Wattenberg MM, Walter DM, Carpenter EL, Feldser DM, et al. Type 1 conventional dendritic cells are systemically dysregulated early in pancreatic carcinogenesis. J Exp Med 2020;217:e20190673.
27. Pombo Antunes AR, Scheyltjens I, Lodi F, Messiaen J, Antoranz A, Duerinck J, et al. Single-cell profiling of myeloid cells in glioblastoma across species and disease stage reveals macrophage competition and specialization. Nat Neurosci 2021;24:595–610.
28. Lun ATL, McCarthy DJ, Marioni JC. A step-by-step workflow for low-level analysis of single-cell RNA-seq data with bioconductor. F1000Research 2016;5:2122. https://pubmed.ncbi.nlm.nih.gov/27909575/.
29. Street K, Risso D, Fletcher RB, Das D, Ngai J, Yosef N, et al. Slingshot: Cell lineage and pseudotime inference for single-cell transcriptomics. BMC Genomics 2018;19:477. https://doi.org/10.1186/s12864–018–4772–0.
30. Van den Berge K, Roux de Bézieux H, Street K, Saelens W, Cannoodt R, Saeys Y, et al. Trajectory-based differential expression analysis for single-cell sequencing data. Nat Commun 2020;11:1–13. https://doi.org/10.1038/s41467–020–14766–3.
31. Zhou Y, Zhou B, Pache L, Chang M, Khodabakhshi AH, Tanaseichuk O, et al. Metascape provides a biologist-oriented resource for the analysis of systems-level datasets. Nat Commun 2019;10:1–10. https://doi.org/10.1038/s41467–019–09234–6.
32. Zhang L, Li Z, Skrzypczynska KM, Fang Q, Zhang W, O'Brien SA, et al. Single-cell analyses inform mechanisms of myeloid-targeted therapies in colon cancer. Cell 2020;181:442–59. http://dx.doi.org/10.1016/j.cell.2020.03.048.

33. Seldeslachts L, Vanderbeke L, Fremau A, Reséndiz-Sharpe A, Jacobs C, Laeveren B, et al. Early oseltamivir reduces risk for influenza-associated aspergillosis in a double-hit murine model. Virulence 2021;12:2493. /pmc/articles/PMC8923074/.
34. Berghen N, Dekoster K, Marien E, Dabin J, Hillen A, Wouters J, et al. Radiosafe micro-computed tomography for longitudinal evaluation of murine disease models. Sci Rep 2019;9:1–10.
35. Marien E, Hillen A, Vanderhoydonc F, Swinnen JV., Vande Velde G. Longitudinal microcomputed tomography-derived biomarkers for lung metastasis detection in a syngeneic mouse model: added value to bioluminescence imaging. Lab Investig 2017;97:24–33.
36. Vande Velde G, Poelmans J, De Langhe E, Hillen A, Vanoirbeek J, Himmelreich U, et al. Longitudinal micro-CT provides biomarkers of lung disease and therapy in preclinical models, thereby revealing compensatory changes in lung volume. Dis Model Mech 2015;9:91–8. /pmc/articles/PMC4728330/.
37. Kurtulus S, Madi A, Escobar G, Klapholz M, Nyman J, Christian E, et al. Checkpoint blockade immunotherapy induces dynamic changes in PD-1 − CD8 + tumor-infiltrating T cells. Immunity 2019;50:181–94. https://pubmed.ncbi.nlm.nih.gov/30635236/.
38. Siddiqui I, Schaeuble K, Chennupati V, Fuertes Marraco SA, Calderon-Copete S, Pais Ferreira D, et al. Intratumoral Tcf1 + PD-1 + CD8 + T cells with stem-like properties promote tumor control in response to vaccination and checkpoint blockade immunotherapy. Immunity 2019;50:195–211. https://pubmed.ncbi.nlm.nih.gov/30635237/.
39. Quezada SA, Jarvinen LZ, Lind EF, Noelle RJ. CD40/CD154 interactions at the interface of tolerance and immunity. Annu Rev Immunol 2004:307–28. https://www.annualreviews.org/doi/abs/10.1146/annurev.immunol.22.012703.104533.
40. Movahedi K, Laoui D, Gysemans C, Baeten M, Stangé G, Van Bossche JD, et al. Different tumor microenvironments contain functionally distinct subsets of macrophages derived from Ly6C(high) monocytes. Cancer Res 2010;70:5728–39.
41. Van Damme H, Dombrecht B, Kiss M, Roose H, Allen E, Van Overmeire E, et al. Therapeutic depletion of CCR8+ tumor-infiltrating regulatory T cells elicits antitumor immunity and synergizes with anti-PD-1 therapy. J Immunother cancer 2021;9:e001749.
42. Zilionis R, Engblom C, Pfirschke C, Savova V, Zemmour D, Saatcioglu HD, et al. Single-cell transcriptomics of human and mouse lung cancers reveals conserved myeloid populations across individuals and species. Immunity 2019;50:1317–34. https://doi.org/10.1016/j.immuni.2019.03.009.
43. Maier B, Leader AM, Chen ST, Tung N, Chang C, LeBerichel J, et al. A conserved dendritic-cell regulatory program limits antitumour immunity. Nature 2020;580:257–62.
44. Yamazaki C, Sugiyama M, Ohta T, Hemmi H, Hamada E, Sasaki I, et al. Critical roles of a dendritic cell subset expressing a chemokine receptor, XCR1. J Immunol 2013;190:6071–82.
45. Qian J, Olbrecht S, Boeckx B, Vos H, Laoui D, Etlioglu E, et al. A pan-cancer blueprint of the heterogeneous tumor microenvironment revealed by single-cell profiling. Cell Res. Springer US; 2020;30:745–62.
46. Di Blasio S, Wortel IMN, van Bladel DAG, de Vries LE, Duiveman-de Boer T, Worah K, et al. Human CD1c(+) DCs are critical cellular mediators of immune responses induced by immunogenic cell death. Oncoimmunology 2016;5:e1192739.
47. Nizzoli G, Krietsch J, Weick A, Steinfelder S, Facciotti F, Gruarin P, et al. Human CD1c+ dendritic cells secrete high levels of IL-12 and potently prime cytotoxic T-cell responses. Blood 2013;122:932–42. http://www.ncbi.nlm.nih.gov/pubmed/23794066.
48. Hughes R, Qian BZ, Rowan C, Muthana M, Keklikoglou I, Olson OC, et al. Perivascular M2 macrophages stimulate tumor relapse after chemotherapy. Cancer Res 2015;75:3479–91.
49. Kiss M, Vande Walle L, Saavedra PHV, Lebegge E, Van Damme H, Murgaski A, et al. IL1β promotes immune suppression in the tumor microenvironment independent of the inflammasome and gasdermin D. Cancer Immunol Res 2021;9:309–23.
50. Eash KJ, Greenbaum AM, Gopalan PK, Link DC. CXCR2 and CXCR4 antagonistically regulate neutrophil trafficking from murine bone marrow. J Clin Invest 2010;120:2423–31.
51. Garg AD, Romano E, Rufo N, Agostinis P. Immunogenic versus tolerogenic phagocytosis during anticancer therapy: mechanisms and clinical translation. Cell Death Differ 2016;23:938–51.
52. Suntharalingam G, Perry MR, Ward S, Brett SJ, Castello-Cortes A, Brunner MD, et al. Cytokine storm in a phase 1 trial of the anti-CD28 monoclonal antibody TGN1412. N Engl J Med 2006;355:1018–28. www.nejm.
53. Vonderheide RH, Burg JM, Mick R, Trosko JA, Li D, Shaik MN, et al. Phase I study of the CD40 agonist antibody CP-870,893 combined with carboplatin and paclitaxel in patients with advanced solid tumors. Oncoimmunology 2013;2:e23033. /pmc/articles/PMC3583942/.
54. Garris CS, Wong JL, Ravetch JV, Knorr DA. Dendritic cell targeting with Fc-enhanced CD40 antibody agonists induces durable antitumor immunity in humanized mouse models of bladder cancer. Sci Transl Med 2021;13:eabd1346.
55. Ataide MA, Komander K, Knöpper K, Peters AE, Wu H, Eickhoff S, et al. BATF3 programs CD8+ T cell memory. Nat Immunol 2020;21:1397–407. http://dx.doi.org/10.1038/s41590–020–0786–2.
56. Gerhard GM, Bill R, Messemaker M, Klein AM, Pittet MJ. Tumor-infiltrating dendritic cell states are conserved across solid human cancers. J Exp Med 2021;218:e20200264.
57. Bosteels C, Neyt K, Vanheerswynghels M, van Helden MJ, Sichien D, Debeuf N, et al. Inflammatory type 2 cDCs acquire features of cDC1s and macrophages to orchestrate immunity to respiratory virus infection. Immunity 2020;52:1039–56.
58. Bourdely P, Anselmi G, Vaivode K, Ramos RN, Missolo-Koussou Y, Hidalgo S, et al. Transcriptional and functional analysis of CD1c+ human dendritic cells identifies a CD163+ subset priming CD8+CD103+ T cells. Immunity 2020;53:335–52.
59. Gutwillig A, Santana-Magal N, Farhat-Younis L, Rasoulouniriana D, Madi A, Luxenburg C, et al. Transient cell-in-cell formation underlies tumor resistance to immunotherapy. bioRxiv 2020;2020.09.10.287441. https://doi.org/10.1101/2020.09.10.287441.
60. Van Overmeire E, Stijlemans B, Heymann F, Keirsse J, Morias Y, Elkrim Y, et al. M-CSF and GM-CSF receptor signaling differentially regulate monocyte maturation and macrophage polarization in the tumor microenvironment. Cancer Res 2016;76:35–42.
61. Simoni Y, Becht E, Fehlings M, Loh CY, Koo S-L, Teng KWW, et al. Bystander CD8+ T cells are abundant and phenotypically distinct in human tumour infiltrates. Nature 2018;557:575–9.
62. Scheper W, Kelderman S, Fanchi LF, Linnemann C, Bendle G, de Rooij MAJ, et al. Low and variable tumor reactivity of the intratumoral TCR repertoire in human cancers. Nat Med 2019;25:89–94.
63. Nowak AK, Cook AM, McDonnell AM, Millward MJ, Creaney J, Francis RJ, et al. A phase 1b clinical trial of the CD40-activating antibody CP-870,893 in combination with cisplatin and pemetrexed in malignant pleural mesothelioma. Ann Oncol 2015;26:2483–90. http://www.annalsofoncology.org/article/S0923753419357187/fulltext.
64. Johnson P, Challis R, Chowdhury F, Gao Y, Harvey M, Geldart T, et al. Clinical and biological effects of an agonist anti-CD40 antibody: a cancer research UK phase I study. Clin Cancer Res 2015;21:1321–8. https://pubmed.ncbi.nlm.nih.gov/25589626/.
65. Siwicki M, Gort-Freitas NA, Messemaker M, Bill R, Gungabeesoon J, Engblom C, et al. Resident Kupffer cells and neutrophils drive liver toxicity in cancer immunotherapy. Sci Immunol 2021;6:eabi7083.